Chinese Journal of Aeronautics, (2019), 32(1): 58–77

Chinese Society of Aeronautics and Astronautics
& Beihang University

Chinese Journal of Aeronautics

cja@buaa.edu.cn
www.sciencedirect.com

Modeling novel methodologies for unmanned aerial systems – Applications to the UAS-S4 Ehecatl and the UAS-S45 Bálaam

Maxime Alex Junior KUITCHE, Ruxandra Mihaela BOTEZ *

ETS, Laboratory of Active Controls, Avionics and AeroServoElasticity LARCASE, Montreal H3C-1K3, Canada

Received 29 March 2018; revised 12 April 2018; accepted 16 April 2018
Available online 14 November 2018

KEYWORDS

Aerodynamics;
Aerospace propulsion;
Flight dynamics;
Unmanned aerial vehicles modeling

Abstract The rising demand for Unmanned Aerial Systems (UASs) to perform tasks in hostile environments has emphasized the need for their simulation models for the preliminary evaluations of their missions. The efficiency of the UAS model is directly related to its capacity to estimate its flight dynamics with minimum computational resources. The literature describes several techniques to estimate accurate aircraft flight dynamics. Most of them are based on system identification. This paper presents an alternative methodology to obtain complete model of the S4 and S45 unmanned aerial systems. The UAS-S4 and the UAS-S45 models were divided into four sub-models, each corresponding to a specific discipline: aerodynamics, propulsion, mass and inertia, and actuator. The "aerodynamic" sub-model was built using the Fderivatives in-house code, which is an improvement of the classical DATCOM procedure. The "propulsion" sub-model was obtained by coupling a two-stroke engine model based on the ideal Otto cycle and a Blade Element Theory (BET) analysis of the propeller. The "mass and the inertia" sub-model was designed utilizing the Raymer and DATCOM methodologies. A sub-model of an actuator using servomotor characteristics was employed to complete the model. The total model was then checked by validation of each sub-model with numerical and experimental data. The results indicate that the obtained model was accurate and could be used to design a flight simulator.

1. Introduction

During recent years, interest in Unmanned Aerial Systems (UAS) has shown an enormous growth in both military and civil aviation. The increased demand has led engineers and designers to search for methods to improve flight performance,[1] especially for long endurance reconnaissance and intelligence missions. However, the validation of a performance improvement technique requires a high number of flight

* Corresponding author.
E-mail address: ruxandra.botez@etsmtl.ca (R.M. BOTEZ).
Peer review under responsibility of Editorial Committee of CJA.

ELSEVIER Production and hosting by Elsevier

https://doi.org/10.1016/j.cja.2018.10.012
1000-9361

tests, which can be very demanding in terms of both time and money. A high-level simulation model provides an alternative solution, allowing engineers to perform numerical calculations to test new aircraft designs or any modifications to existing ones in a simulation environment.[2]

Designing a model or realizing an aircraft simulator may, under certain conditions, result in aberrant results, including numerical instability due to the successive error increases. To cope with this difficulty, the aircraft model is divided into sub-models. The general model of the aircraft depends on its geometry, its systems and the environmental factors. Therefore, its overall architecture is composed of aerodynamics, propulsion and actuation systems, as well as its mass and inertia. Thus, the modelling procedure for an aircraft is a collection of methods for estimation of each sub-model. Several studies have been conducted to examine this methodology.

Jodeh et al.[3] developed a nonlinear simulation model to estimate the flight dynamics of the Rascal 110, with its aerodynamic model designed using the DATCOM procedure. The propeller model was based on the airfoil characteristics while the engine model consisted of a linear lookup table. The mass and inertia analyses were conducted by the experimental pendulum method. Al-Radaideh designed and built a test bed for the ARF60 AUS-UAV.[4] The model was constructed under Simulink using Aerosim and Aeroblockset to facilitate the flight control system development. The aerodynamics was modelled using linear estimation based on the aircraft's geometry. The propulsion model used a transfer function with the throttle command as input, and the RPM of the engine and the thrust produced by the propeller as outputs. This model was used to test autopilot behaviour. The results have shown that the outputs were very close to the command values.

A procedure to model small unmanned vehicles at high angles of attack was presented by Selig.[5] This methodology was developed for UAV/Radio-Controlled aircraft (RC). The UAV/RC was divided into basic components, such as wing, horizontal tail and vertical tail, in order to evaluate their interaction effects. The aerodynamic analysis was performed using strip theory while the propeller model was estimated from blade element momentum theory using PROPID code.[6] The aircraft model was implemented in the Flight Simulator (FS-1) to determine its flight dynamics at stall condition.

Elharouny et al.[7] provided a procedure for modelling small UAV. This procedure was applied on a Sky Raider Mach 1. The aerodynamic modelling was performed by coupling Xfoil[8] to determine the airfoil aerodynamics characteristic and DATCOM to estimate the overall aerodynamic model of the UAV. The propulsion model consisted of evaluating the thrust performance of the UAV. It was estimated experimentally using a spring scale to measure the thrust force along with a set of throttle command and incoming wind speed. The moment of inertia and the center of gravity were obtained from a pendulum method while the mass were determined using a balance. The resulting model was used for control design tasks.

Kamal et al.[2] presented a flight simulation model for a small commercial off-the-shelf UAV/RC, the "tiger Trainer". The structural model consisted in determining the mass, the center of gravity and the moment of inertia of the UAV. The mass was obtained using an accurate digital scale and the center of gravity was estimated from a moment balance about the nose wheel. The pendulum method was thus applied to experimentally evaluate the UAV moment of inertia. The propulsion system consisted of a piston-propeller engine. The propulsion modelling was separated into the propeller analysis and the engine dynamic estimation. The propeller analysis was performed experimentally in a low speed wind tunnel to measure thrust and power performance from static condition to windmill regime. The engine dynamic was built from a black box using pulse on the throttle as input and engine rotation speed as output. The aerodynamic characteristics were obtained, in the first step, by analysing the similarity of the wing airfoil with conventional airfoil as Clark-Y. In the second step, DATCOM was used to obtain aerodynamic behaviour of the entire UAV. The actuator was modelled from an identification process on a servomotor. This methodology required a time history of the rotational angle of the servomotor as function of a signal inputs which were measured experimentally. The complete six DoF nonlinear model of the UAV was assembled using MATLAB/Simulink. The model was verified, for a horizontal steady flight, on its longitudinal and lateral dynamic. The results showed a good agreement with the experimental flight test.

Raymer[9] developed a code called RDS, dedicated to the development and analysis of aerospace vehicles. It contained a sizing code based on Roskam[10–12] and features analysis modules for the aerodynamics, mass and inertia and propulsion models. The program was applied on a STOVL jet aircraft.[13] Aerodynamic behaviour was estimated using classical techniques from Ref.,[11] while the drag, the maximum lift and the control derivatives were estimated using the DATCOM procedure.[14] The mass and inertia properties were obtained using a statistical method based on the type of aircraft, and were further adjusted based on the aircraft composite materials and systems. The propulsion models were estimated from a default engine data on which corrections were applied. These corrections were defined as the differences between the reference and the actual inlet recovery pressure, the actual bleed coefficient, and the installed inlet drag.

The Systems Engineering and Aircraft Design Group of Delft University of Technology developed a knowledge-based design software called the Design Engineering Engine (DEE).[15] The software includes a tool, the Flight Mechanics Model (FMM), which analyses the flight dynamics of an aircraft. The FMM combines sub-models for aerodynamics, structure and propulsion analysis into one single aircraft model. These sub-models are physical-based or empirical. The DEE has been used in several academic and industrial research projects. In the European project MOB (Multidisciplinary Optimisation of a Blended wing-body), the DEE was used to achieve a distributed computational design framework for the multidisciplinary design and optimisation of a blended wing-body freighter.[16] The TAIL Optimization and Redesign in a Multi Agent Task Environment (TAILORMATE) project[17,18] a collaboration project with Airbus, used the DEE software for the fully automatic redesign of the vertical tail of a large passenger aircraft.

The simulating aircraft stability and control characteristics for use in conceptual design (SimSAC)[19] project was a FP6 European project with the aim of developing a tool for modelling and simulating aircraft stability and control. The Computerized Environment for Aircraft Synthesis an Integrated Optimization Methods, Computerized Environment for

Aircraft Synthesis an Integrated Optimization Methods (CEASIOM) was the resulting software of this project. CEASIOM is a framework tool that integrated multi-discipline methods dedicated to the modelling and the analysis of fixed-wing aircraft. CEASIOM contains 8 significant modules: the Aircraft Builder (AcBuilder) and the Surface Modeller (SUMO) allows to build geometry for aerodynamic calculation. These tools can generate surface and volume mesh useful for CFD analysis. The weight and balances module estimates the mass the inertia and the position of the center of gravity using the geometry data of the aircraft. Four methods are provided to estimate mass and inertia: the Howe,[20] Torenbeek,[21] Raymer[22] and the DATCOM methods. The aerodynamic model builder module combines computational, analytical and semi-empirical methods to obtain the aerodynamic model of the aircraft. Depending on the accuracy needed, the user can choose between low cost methods as DATCOM and Vortex Lattice Method (VLM), and time demanding methods as Euler and Reynolds Averaged Navier-Stokes (RANS) analysis, to perform aerodynamics calculation. The next generation aero-structural sizing module perform an aero-structural analysis by giving a complete understanding of aerodynamic, structure and aero elastic interaction for several flight conditions. The propulsion module uses the thrust data as a function of Mach number and altitude to construct a propulsion database useful for stability and control analysis. The Simulation and Dynamic Stability Analyser (SDSA) module provides stability analysis with eigenvalues estimation of the linearized model and it also provides a six degree of freedom flight simulation. The Flight Control System Design Toolkit (FCSDT) is useful to design a Stability Augmentation System (SAS) and a flight control system based on a LQR approach. These modules generate enough data to build a six Degree of Freedom flight simulator. The Ranger 2000 trainer was modelled using CEASIOM[19] to study the rudder free effect at low attitude and speed when a lateral gust is encounter. The results show that at low attitude and speed, the oscillation of the rudder and the sideslip cannot be damped by the yaw rate. Thus the aircraft loses altitude until it crashes. These results were confirmed by experimental flight tests.

Table 1 shows the different aircraft modelling procedures and the corresponding methodologies. This paper describes a procedure for modelling the both Unmanned Aerial System UAS-S4 and UA-S45, designed and manufactured by Hydra Technologies. They provide surveillance and security capabilities for military and civilian purposes.[24] General information regarding the UAS-S4 and the UAS-S45 is presented in Tables 2 and 3, respectively, and Figs. 1 and 2 show their respective images.

In this paper, the architecture of each UAS integrates sub-models to evaluate the aerodynamics, propulsion, actuation, the mass and inertia. The aerodynamic sub-model was obtained with Fderivatives code, an improvement of the DAT-

Table 2 General Characteristics of the UAS-S4.

Specification	Value
Wing span (m)	4.2
Wing area (m^2)	2.3
Total length (m)	2.5
Mean aerodynamic chord (m)	0.57
Empty weight (kg)	50
Maximum take-off weight (kg)	80
Loitering airspeed (knot)	35
Maximum speed (knot)	135
Service ceiling (ft)	15000
Operational range (km)	120

Note: 1 ft = 304.8 mm; 1 knot = 1.852 km/h.

Table 3 General Characteristics of the UAS-S45.

Specification	Value
Wing span (m)	6.11
Wing area (m^2)	2.72
Total length (m)	3.01
Mean aerodynamic chord (m)	0.57
Empty weight (kg)	57
Maximum take-off weight (kg)	79.6
Loitering airspeed (knot)	55
Service ceiling (ft)	20000
Operational range (km)	120

Table 1 Aircraft modelling methods.

Reference	Aircraft	Method			
		Aerodynamic	Propulsion	Structure	Actuator
Jodeh[23]	Rascal 110	DATCOM	Airfoil analysis	Pendulum	
Al-Radaideh et al.[4]	ARF60 AUS-UAV	Linear estimation from aircraft geometry	1st order transfer function	Pendulum	
Selig[5]	UAV/RC	Strip theory	BET		
Elharouny et al.[7]	Sky Raider Mach 1	Xfoil, DATCOM	Experimental measurement	Balance measurement, pendulum	
Kamal et al.[2]	Tiger Trainer	Airfoil analysis, DATCOM	Wind tunnel test, black box identification	Balance measurement, pendulum	Black box identification
Raymer and McCrea[13]	STOVL Jet Aircraft	Roskam, DATCOM, VLM	Default engine corrected	Statistical	
Rizzi[19]	General Aircraft	DATCOM, VLM, RANS, EULER	Interpolation from database	Howe, Torenbeek, Raymer, DATCOM	

Fig. 1 Hydra technologies UAS-S4 Ehecatl.

Fig. 2 Hydra technologies UAS-S45 Bàlaam.

COM procedure. This code was developed in-house at our Research Laboratory in Active Controls, Avionics and Aeroservoelasticity of the ETS. Its main advantage is related to the need of a minimum number of geometrical data to estimate the aircraft aerodynamic coefficients and their corresponding stability derivatives.[25] The aerodynamic coefficients of each UAS, obtained using Fderivatives code, were compared with those calculated with the DATCOM procedure, the Vortex Lattice Method (VLM) on TORNADO and the Computational Fluid Dynamics (CFD)[26] analysis on ANSYS Fluent.

The propulsion sub-model was obtained by coupling two-stroke engine modelling and a numerical analysis of the propeller. The two-stroke model is based on the Otto cycle thermodynamic equation, and on the geometrical characteristics of the engine. The torque produced by the engine as well as the fuel consumption and the rotation speed of the crankshaft were determined. The propeller analysis estimated the thrust and propeller efficiency as a function of the advance ratio from an in-house blade element theory code. The two-stroke engine model was compared to the manufacturer's data, and the propeller analysis was compared to a CFD analysis on ANSYS Fluent.

Each UAS model was completed with the sub-model of an actuator. Each actuator is a servomotor, therefore a controlled DC motor was used for its modelling. The structural sub-model was calculated using the Raymer and the DATCOM methodologies. The aerodynamic sub-model is explained in Section 2, the propulsion sub-model in Section 3, the actuator sub-model in Section 4, and the structural model in Section 5. Results are given in Section 6 and are followed by a conclusion section. Results have been validated using different modelling and simulation approaches including experimental data (for actuator and structure) for-each sub-model of the UAS.

2. Aerodynamic sub-model

The aerodynamic sub-model deals with the estimation of an aircraft's aerodynamic behaviour. To accurately predict the aerodynamic forces and moments that act on an aircraft in flight, it is necessary to describe the pattern of flow around the aircraft configuration.[27]

The DATCOM procedure is one of the best collections of semi-empirical equations for aerodynamic coefficients and stability derivative calculations. This tool is used for the evaluation of aerodynamic coefficients for preliminary aircraft design, and provides equations for various aircraft configurations and flight regimes.[28] The calculation method used in DATCOM is based on the summation of the contributions of all of an aircraft's components along with their interaction effects. Although the DATCOM procedure can create a good aerodynamic model, it also presents some weaknesses. This procedure does not provide a methodology for estimating the zero lift angle of attack or the zero lift pitch moment for an airfoil or for an asymmetrical fuselage. The procedure does not take into account the aerodynamic twist of the wing in the calculation of the lift-curve slope of the wing. In addition, the contribution of the engine nacelles is neglected.

In this context, our LARCASE team at ETS has developed a new code called Fderivatives. Fderivatives contains new equations and methods that have been added to DATCOM's classical procedure to improve the aerodynamic coefficients and stability derivative calculation for flying subsonic regime.[25,28,29]

2.1. Fderivatives' improvements

Fderivatives is an in-house code designed as a collection of semi-empirical methodologies for determining aerodynamic coefficients and stability derivatives. The code includes a number of procedures such as those in DATCOM, with improvements in both the theoretical equations and in calculation methodologies. All of the improvements and the description of the code are given in Refs.[25,28–30] The main improvements proposed in the Fderivatives code with respect to the DATCOM procedure are realised in the calculation of the airfoil lift-curve slope $c_{L\alpha}$, the zero lift angle of attack α_0 and the zero lift pitch moment c_{m0}, in the zero lift angle of attack α_{0f}, for an asymmetrical fuselage, and in the maximum lift coefficient of the wing $C_{L\max}$.

2.1.1. Lift-curve slope, zero lift angle of attack and zero lift pitching moment of airfoil

The lift-curve slope of the airfoil, $c_{L\alpha}$, is one of the most important parameters for the calculation of an aircraft's aerodynamic coefficients. In Fderivatives, the lift-curve slope (lift coefficient derivative with respect to α) is estimated for an ideal flow, and then is corrected for viscous and compressible flow conditions:

$$c_{L\alpha} = \frac{1.05}{\beta_{PG}} \left[\frac{c_{L\alpha}}{(c_{L\alpha})_{\text{theory}}} \right] (c_{L\alpha})_{\text{theory}} \tag{1}$$

where $(c_{L\alpha})_{\text{theory}}$ is the lift-curve slope of the airfoil for inviscid and incompressible flow. Then,

$$(c_{L\alpha})_{\text{theory}} = 6.28 + 4.7\left(\frac{t}{c}\right)_{\max}(1 + 0.00375\Phi_{\text{TE}}) \quad (2)$$

where $\left(\frac{t}{c}\right)_{\max}$ is the maximum thickness of the airfoil, and Φ_{TE} is the trailing edge angle calculated in degrees.

The following factors are incorporated to correct for the compressible and viscous flow conditions:

β_{PG} is the Prandtl-Glauert correction factor for compressible flow, and it depends upon the Mach number Ma according to the following expression:

$$\beta_{\text{PG}} = \sqrt{1 - Ma^2} \quad (3)$$

$\frac{c_{L\alpha}}{(c_{L\alpha})_{\text{theory}}}$ is a correction factor for viscous flow that is a function of the Reynolds number Re and of the trailing edge geometry of the profile[31]:

$$\frac{c_{L\alpha}}{(c_{L\alpha})_{\text{theory}}} = 1 - \left(\ln\frac{Re}{10^5}\right)^n\left[0.232 + 1.785\tan\left(\frac{\Phi_{\text{TE}}}{2}\right) - 2.95\tan^2\left(\frac{\Phi_{\text{TE}}}{2}\right)\right] \quad (4)$$

where the term n can be found with:

$$n = -1 + \frac{5}{2}\tan\left(\frac{\Phi_{\text{TE}}}{2}\right) \quad (5)$$

The zero lift angle of attack α_0 and the zero lift pitching moment c_{m0} are obtained by utilizing the theory developed by Pankhurst.[32] Pankhurst established a calculation procedure in which α_0 and c_{m0} are written as linear combinations of their values of the y-axis Z_e values of an airfoil's upper surface, and of the Z_i values of its lower surface. The parameters Z_e and Z_i correspond to a finite number of chosen points.

$$\begin{cases} \alpha_0 = -\sum_j A_j(Z_e + Z_i)_j \\ c_{m0} = -\sum_j B_j(Z_e + Z_i)_j \end{cases} \quad (6)$$

where A_j and B_j are correlation coefficients depending on their x-axis values on the chord.[29,30] The compressibility, and the Reynolds number effects on the zero lift angle of attack α_0 and on the zero lift pitching moment c_{m0} are neglected as specified in Ref.[33]

2.1.2. Maximum lift coefficient of wing

Derivatives code uses two methods to estimate a wing's maximum lift coefficient, depending on the type of the wing.

In the "first" method, for a constant airfoil configuration, the wing is divided into ten sections. For each section, a lift coefficient distribution is calculated thereby allowing its nonlinear twisted wing values to be taken into account.[25] The maximum lift coefficient of the airfoil, $c_{L\max}$, is calculated in the section where the lift coefficient has the highest value. The equation developed by Phillips and Alley[34] is then used:

$$c_{L\max} = \left(\frac{c_L}{c_{L\max}}\right)_{\substack{\theta=0\\ \Lambda=0}} k_{L\Lambda}(c_{L\max} - k_{L\theta}C_{L\alpha}\theta) \quad (7)$$

where θ is the twist of the wing, Λ is the sweep angle of the wing, $k_{L\Lambda}$and $k_{L\theta}$ are respectively the sweep and the twist correction factor, $c_{L\max}$ is the maximum lift coefficient of the airfoil calculated in the section where the lift coefficient has the highest value, $C_{L\alpha}$ is the lift-curve slope of the wing, and $\left(\frac{c_L}{c_{L\max}}\right)_{\substack{\theta=0\\ \Lambda=0}}$ is a correction factor of the maximum lift coefficient for unswept and untwisted wing sections.

In the "second" method, for a wing whose airfoil changes along the span, Roskam's method[10,11] is applied. The maximum lift coefficient of the wing is assumed to be proportional to the maximum lift coefficient of the airfoil at the tip and at the root of the wing:

$$C_{L_{\max}} = f\cos(\Lambda_{c/4})\frac{(c_{L_{\max}})_{\text{tip}} + (c_{L_{\max}})_{\text{root}}}{2} \quad (8)$$

where $(c_{L\max})_{\text{tip}}$ and $(c_{L\max})_{\text{root}}$ are the maximum lift coefficients of the airfoil at the tip and at the root of the wing, $\Lambda_{c/4}$ is the quarter chord sweep angle, and f is a correction coefficient dependent upon the taper ratio r:

$$f = -0.117r + 0.997 \quad (9)$$

2.1.3. Zero-lift angle of attack of an asymmetrical fuselage

The procedure to estimate the zero lift angle of attack, α_{0f}, is based on the thin airfoil theory. Jacobs et al.[33] proposed an equation for the determination of α_{0f} by using the mean camber line:

$$\alpha_{0f} = \int_0^l \frac{\xi(x)}{l} f\left(\frac{x}{l}\right) \quad (10)$$

where

$$f\left(\frac{x}{l}\right) = -\frac{1}{\pi}\cdot\frac{1}{\left(1 - \frac{x}{l}\right)\sqrt{\frac{x}{l} - \left(\frac{x}{l}\right)^2}} \quad (11)$$

In Eqs. (10) and (11), l is the length of the fuselage, x is the position on the mean camber line, and $\xi(x)$ is the mean camber line defined by:

$$\xi(x) = \frac{1}{2}[Z_i(x) + Z_e(x)] \quad (12)$$

Therefore, the fuselage can be replaced by a body of revolution with the same longitudinal distribution of the section as the original one.[35]

2.2. Fderivatives' logical scheme description

Fderivatives' graphical interface, produced at the LARCASE, ETS, allows users to calculate the aircraft stability from its geometrical data.[25] Its main window with its sub-windows is presented in Fig. 3. The Fderivatives code's logical scheme is given in two steps, as illustrated in Fig. 4. The first step regards the selection of the aircraft configuration (Wing (W), Wing-Body (WB) or Wing-Body-Tail (WBT)), the type of planform (straight-tapered or non-straight tapered wing), and the flight conditions (altitude, Mach number and angle of attack).[28] For each aircraft configuration, following parameters are needed: area, aspect ratio, taper ratio, and sweepback angle, for the wing, the horizontal and vertical tails, as well as their respective airfoil. The code also takes as inputs, the airfoil coordinates of the root, the tip and the mean aerodynamic chords as wells as the parameters for the fuselage and nacelle.

Estimating the aerodynamic coefficients and the stability derivatives for a specific flight condition is the second step in the Fderivatives code. For each UAS, the wing-body-tail configuration was selected as the best one among the possible combinations (wing, wing-tail etc.) with the aim to obtain reliable results. The aerodynamic model was designed to analyse or to modify each component of the UAS separately, and their

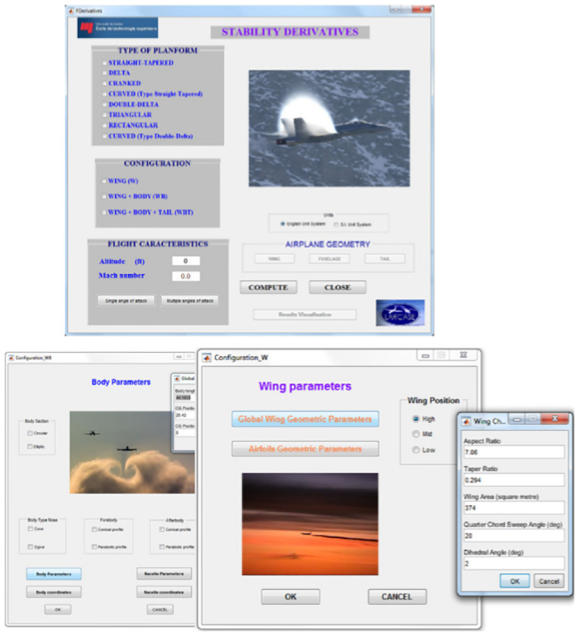

Fig. 3 Main window and sub-windows of Fderivatives code.

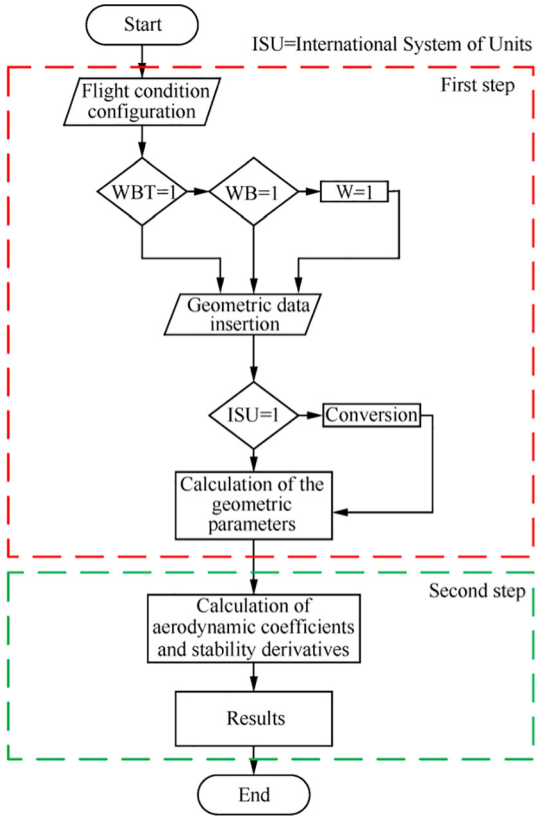

Fig. 4 Logical scheme of Fderivatives code.

interactions effects. Therefore, each UAS will be divided into 5 components: the "Wing-Body", the "Tail", the "control surface", the "propulsion" and the "ground-effect" as shown in Fig. 5. The Fderivatives code does not calculate the control

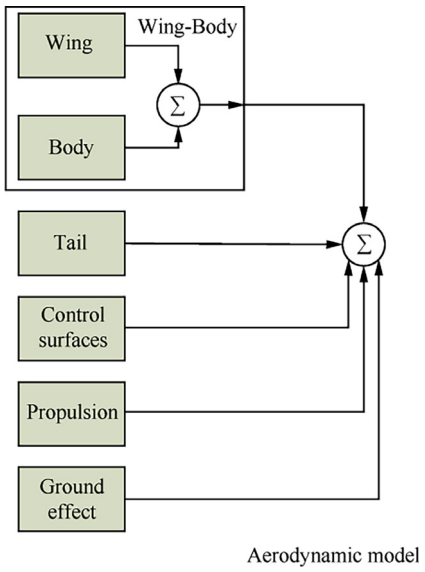

Fig. 5 UAS aerodynamic model design.

surface derivatives, the ground and the propulsion effects. Therefore, these contributions were estimated using the DATCOM methodology.[14]

2.3. VLM using TORNADO code

The VLM is a numerical method to estimate flow dynamic around a lifting surface. It is an effective method to solve problems of incompressible, irrotational and inviscid flows.[36] The VLM is based on the lifting line surface theory. The lifting surfaces are modelled by a zero-thickness solid surface and represented by a grid on which horseshoe vortexes are superimposed at a control point (75% of the chord) (see Fig. 6).

Because of the fact that each panel of the grid is considered as "planar", the Biot-Savart law can be applied to calculate the velocity induced by each horseshoe,[37] with:

$$\boldsymbol{V} = \frac{\Gamma}{4\pi} \cdot \frac{\boldsymbol{r}_1 \times \boldsymbol{r}_2}{|\boldsymbol{r}_1 \times \boldsymbol{r}_2|^2} \left[\boldsymbol{r}_0 \left(\frac{\boldsymbol{r}_1}{|\boldsymbol{r}_1|} - \frac{\boldsymbol{r}_2}{|\boldsymbol{r}_2|} \right) \right] \tag{13}$$

where Γ is the vortex intensity, $\boldsymbol{r}_1$ and $\boldsymbol{r}_2$ are the vectors from the starting and the ending points of the vortex segment to the random point in space, $\boldsymbol{r}_0$ is the vector along of the vortex segment.

For each of the control points in the lattice, the velocities induced by the other panels are summed, leading to a set of equations for the horseshoe vortex (located at the control point), that satisfies the boundary condition of "no flow through the wing".[27] The local velocities calculated by these equations are used to further compute the pressure difference between the upper and lower surfaces of the airfoil. The integration of these pressures leads to obtain the aerodynamics forces and moments.

The TORNADO code was used to apply the VLM to the UASs. TORNADO software is useful for research, education and teaching purposes. It uses VLM to model subsonic potential flow around a lifting surface. The general equations used in TORNADO code were developed by Moran.[38] Since

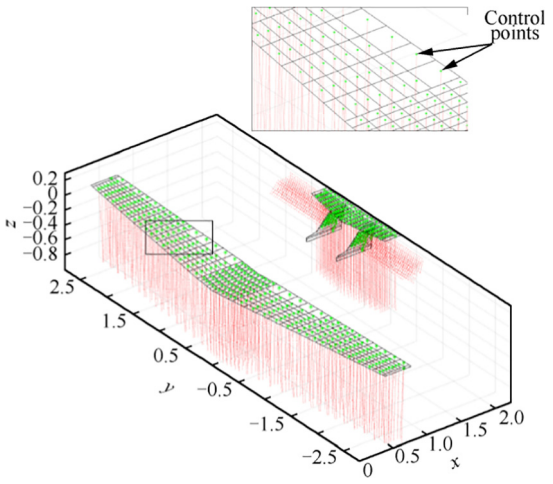

Fig. 6 Panels and controls points modelling using the VLM.

TORNADO computes inviscid flow equations, it does not model the boundary layer. Therefore, the code does not provide the skin friction component of the drag coefficient. In addition, since TORNADO uses a planar approximation of lifting surfaces, it does not take into account the aerodynamic contributions of an aircraft's fuselage.

2.4. CFD methodology with ANSYS Fluent

The CFD analysis in ANSYS Fluent was performed to obtain the aerodynamic sub-model of the UASs. In ANSYS Fluent, the fluid dynamics respects the fundamental principles of mass, momentum and energy conservation that are expressed through the Navier-Stokes equations. For the turbulent flows, the flow variables were decomposed into their time-average values and their fluctuating components. The Reynold stress tensor and the turbulent heat flux terms were related to the average flow variables using the Boussinesq eddy-viscosity hypothesis.[39] These assumptions lead to the following RANS equations:

$$\frac{\partial \rho}{\partial t} + \frac{\partial}{\partial x_j}\left(\rho U_j\right) = 0 \tag{14}$$

$$\frac{\partial}{\partial t}\left(\rho U_i\right) + \frac{\partial}{\partial x_j}\left(\rho U_j U_i\right) = -\frac{\partial P}{\partial x_i} + \frac{\partial}{\partial x_i}\left[\mu_{\text{eff}}\left(\frac{\partial U_i}{\partial x_j} + \frac{\partial U_j}{\partial x_i}\right) - \frac{2}{3}\mu_{\text{eff}}\frac{\partial U_k}{\partial x_k}\delta_{ij}\right] \tag{15}$$

$$\frac{\partial}{\partial t}\left(\rho H\right) - \frac{\partial P}{\partial t} + \frac{\partial}{\partial x_j}\left(\rho U_j H\right) = \frac{\partial}{\partial x_j}\left[\lambda\frac{\partial T}{\partial x_j} + \frac{\mu_t}{Pr_t}\cdot\frac{\partial h}{\partial x_j}\right] + \frac{\partial}{\partial x_j}\left\{U_i\left[\mu_{\text{eff}}\left(\frac{\partial U_i}{\partial x_j} + \frac{\partial U_j}{\partial x_i}\right) - \frac{2}{3}\mu_{\text{eff}}\frac{\partial U_k}{\partial x_k}\delta_{ij}\right] + \mu\frac{\partial k}{\partial x_j}\right\} \tag{16}$$

where ρ is the fluid density, U_i are the velocity components, P is the sum of the static pressure and the $(2\rho\delta_{ij}k)/3$ term resulted from the Boussinesq hypothesis, μ_{eff} is the effective viscosity, which is the sum of the molecular viscosity μ and the turbulent viscosity μ_t, H is the total enthalpy, T is the fluid temperature, δ_{ij} is the Kronecker delta function, λ is the thermal conductivity, Pr_t is the turbulent Prandtl number, h is the static enthalpy and k is the turbulent kinetic energy.

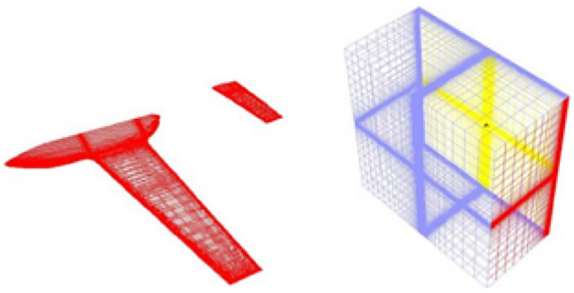

Fig. 7 Mesh model of the UAS-S4 for CFD analysis in ANSYS Fluent.

The k-ω model was used as a closure of the RANS equations. This model achieves high accuracy for boundary layers with adverse pressure gradient, and can be easily integrated into viscous sub-layers without any additional damping function.[40,41] Although the k-ω model has some weakness for flows with free stream boundaries, it can still give good estimation for general subsonic flows.[41]

The k-ω model estimates the turbulence kinetic energy k and the specific rate of dissipation ω by adding two more equations to the RANS equations[41]:

$$\frac{\partial}{\partial t}\left(\rho k\right) + \frac{\partial}{\partial x_j}\left(\rho U_j k\right) = \rho P_k - \beta^* \rho\omega k + \frac{\partial}{\partial x_j}\left[\left(\mu + \sigma_k\mu_t\right)\frac{\partial k}{\partial x_j}\right] \tag{17}$$

$$\frac{\partial}{\partial t}\left(\rho\omega\right) + \frac{\partial}{\partial x_j}\left(\rho U_j \omega\right) = \frac{\gamma\omega}{k}P_k - \beta\rho\omega^2 + \frac{\partial}{\partial x_j}\left[\left(\mu + \sigma_\omega\mu_t\right)\frac{\partial\omega}{\partial x_j}\right] \tag{18}$$

In Eqs. (17) and (18), ω is the specific rate of dissipation, P_k is the turbulent kinetic energy due to mean velocity gradients, and β, γ, σ_k, and σ_ω are the model's constants.

The CFD analysis using ANSYS Fluent was only performed on the UAS-S4. In order to use the partial differential Eqs. (14)–(18), a structured and fine mesh of the UAS-S4 was performed using the ICEM-CFD software. The mesh was composed of 4424844, 4520132 nodes (Fig. 7).

3. Propulsion system

Each of the UAS-S4 and the UAS-S45 use two propeller engines. Propellers are the most important parts of propulsion systems. Each blade of a propeller has an airfoil. Fig. 8 shows the model proposed in order to estimate the propulsion system.

It is composed by two main boxes. The "2-stroke engine" box takes as inputs the atmospheric pressure and temperature, density of the air, the throttle positon and the rotational speed to estimate torque outputs produced by the engine and its fuel flow. The "propeller" box calculates the thrust and the torque

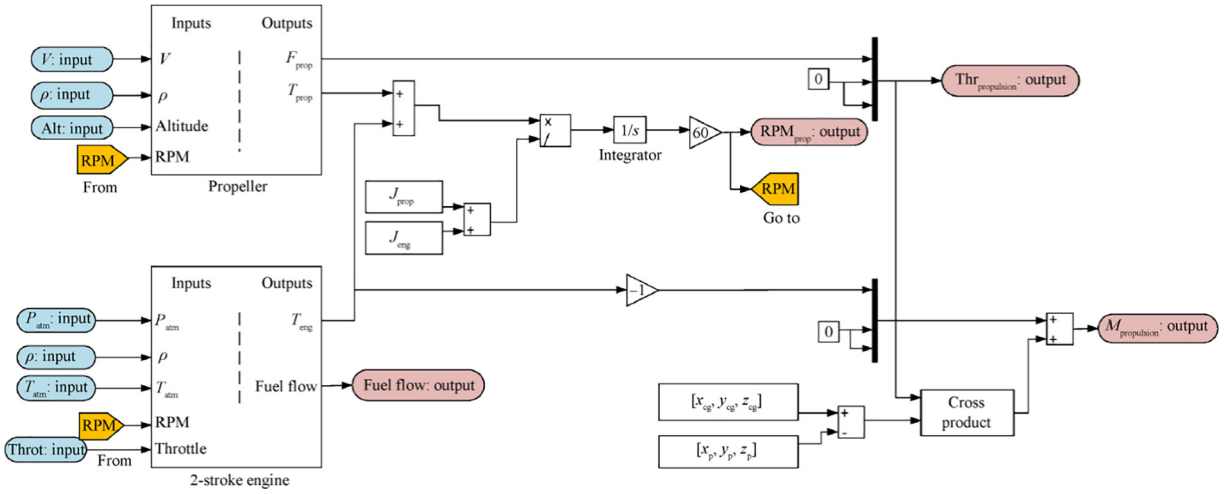

Fig. 8 Model proposed for the propulsion system of each UAS.

outputs by using the airspeed, the rotational speed and the altitude of the flight inputs. The thrust produced by the propulsion system is the same as the thrust produced by the "propeller" box:

$$\mathrm{Thr}_{\mathrm{propulsion}} = F_{\mathrm{prop}} \tag{19}$$

where $\mathrm{Thr}_{\mathrm{propulsion}}$ is the thrust produced by the propulsion system and F_{prop} is the thrust produced by the propeller.

The moment produced by the propulsion system is related to the torques output produced by the engine and the propeller using:

$$M_{\mathrm{propulsion}} = \begin{bmatrix} x_{\mathrm{cg}} - x_{\mathrm{p}} \\ y_{\mathrm{cg}} - y_{\mathrm{p}} \\ z_{\mathrm{cg}} - z_{\mathrm{p}} \end{bmatrix} \begin{bmatrix} Q_{\mathrm{eng}} \\ 0 \\ 0 \end{bmatrix} - Q_{\mathrm{prop}} \tag{20}$$

where x_{cg}, y_{cg}, z_{cg} define the 3D position of the center of gravity of the aircraft, x_{p}, y_{p}, z_{p} define the 3D position of the engine, Q_{eng} is the torque produced by the engine, and Q_{prop} is the torque produced by the propeller.

The rotational speed of the engine is calculated from the Newton's second law for the rotational motion:

$$\mathrm{RPM}_{\mathrm{prop}} = 60 \int \frac{Q_{\mathrm{eng}} + Q_{\mathrm{prop}}}{J_{\mathrm{eng}} + J_{\mathrm{prop}}} \tag{21}$$

where $\mathrm{RPM}_{\mathrm{prop}}$ is the rotational speed of the propeller, J_{eng} and J_{prop} are respectively the inertia of the engine, and of the propeller.

The following sections detail the methodologies applied to determine the outputs of the propeller and the 2-stroke engine boxes.

3.1. Propeller analysis

The propellers' performance analyses were carried using the "blade element theory". The blade element theory is a methodology used to estimate the thrust of a propeller by dividing its blade into segments called "blade elements".[42]

Each segment (blade element) is treated as an airfoil, for which the aerodynamic lift and drag forces are calculated according to the local flow conditions on the segment:

$$\mathrm{d}L = \frac{1}{2}\rho V_{\mathrm{E}}^2 c(r) C_L \mathrm{d}r \tag{22}$$

$$\mathrm{d}D = \frac{1}{2}\rho V_{\mathrm{E}}^2 c(r) C_D \mathrm{d}r \tag{23}$$

where $\mathrm{d}L$ and $\mathrm{d}D$ are the differential lift and drag forces on the blade element, $c(r)$ is the chord at the blade station r, ρ is the air density, and V_{E} is the effective resultant velocity which is given by:

$$V_{\mathrm{E}} = \sqrt{(V_{\mathrm{in}} + V)^2 + (\Omega r_{\mathrm{d}})^2} \tag{24}$$

where Ω is the angular velocity of the propeller and r_{d} is the distance from the hub to the blade element as seen on Fig. 9; V is the airspeed of the aircraft and $V_{\mathrm{in}}$is the induced velocity obtained from the momentum theory. C_L and C_D are respectively the airfoil lift and drag coefficients of the blade element.

Three-dimensional scanning was used to obtain the airfoil sections composing the propeller blade. The section lift and drag coefficients were then determined for a range of angles of attack from -10° to 10° and a range of Reynolds numbers from 5×10^4 to 100×10^4. These coefficients were estimated using Xfoil software,[8] and are presented in Fig. 10. The coefficients were evaluated for the angle of attack α:

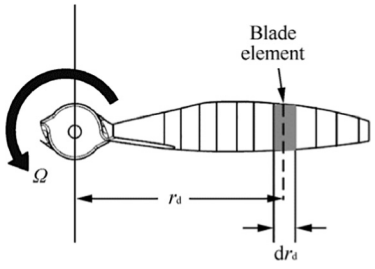

Fig. 9 Blade element representation used in the blade element theory.

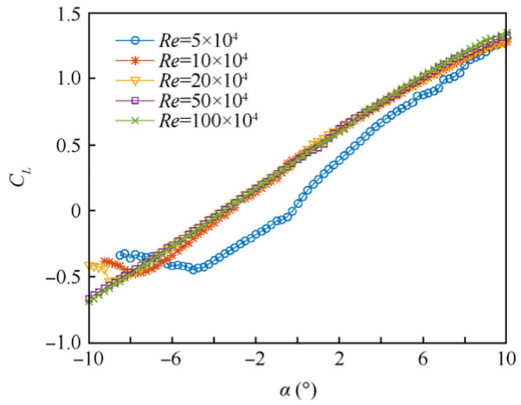

(a) Lift coefficient vs angle of attack

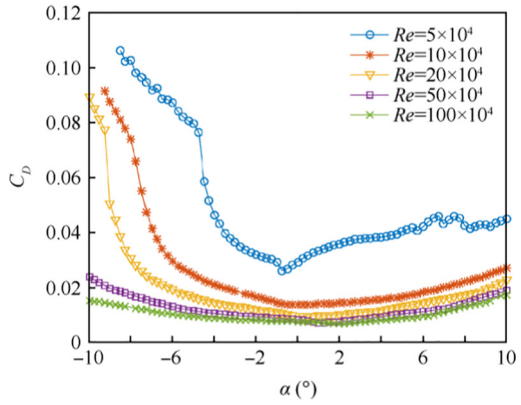

(b) Drag coefficient vs angle of attack

Fig. 10 Lift and drag coefficients' variation with the angle of attack for the airfoil of the propeller.

$$\alpha = \beta - \phi - \alpha_i + \alpha_0 \tag{25}$$

where β is the angle between the zero lift line and the rotation plane, also called the pitch angle, ϕ is the helix angle, α_i is the induced angle of attack obtained from the momentum theory, α_0 is the zero lift angle of attack of the airfoil, as seen on Fig. 11.

The summation of the aerodynamic forces of each element allows to evaluate the properties of the complete propeller.

$$T = N_B \int_{R_{hub}}^{R} dL\cos(\phi + \alpha_i) - N_B \int_{R_{hub}}^{R} dD\sin(\phi + \alpha_i) \tag{26}$$

$$Q = N_B \int_{R_{hub}}^{R} r_d dL\sin(\phi + \alpha_i) - N_B \int_{R_{hub}}^{R} r_d dD\cos(\phi + \alpha_i) \tag{27}$$

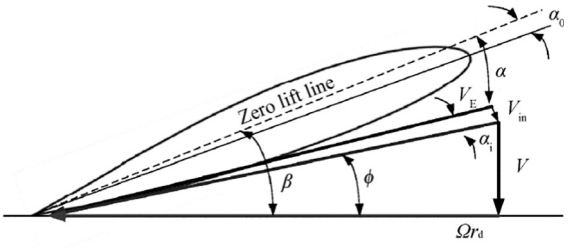

Fig. 11 Angles and velocity of the propeller.

where T and Q are the thrust and torque produced by the propeller, N_B is the number of blades, R is the tip radius and R_{hub} is the hub radius of the propeller. From the thrust and torque determined with Eqs. (26) and (27), the thrust and torque coefficients as well as the efficiency of the propeller were obtained using:

$$C_T = \frac{T}{\rho n^2 d^4} \tag{28}$$

$$C_Q = \frac{Q}{\rho n^2 d^5} \tag{29}$$

$$\eta = J\frac{C_T}{2\pi C_Q} \tag{30}$$

where n is the angular velocity of the propeller, d is the diameter of the propeller and J is the advance ratio expressed by:

$$J = \frac{V}{nd} \tag{31}$$

The thrust coefficient and the efficiency of the propeller obtained from the blade element theory were validated by comparing them with those obtained from a CFD analysis using ANSYS-Fluent (see Fig. 12).

In the first step, the domain in which the calculations were performed was meshed. The chosen domain for the fluid flow is a cylinder, the most suitable and the most conventionally-used domain for a CFD analysis on a propeller. In order to reduce the execution time, the principle of the Multiple Reference Frame (MRF) approach was applied. This approach consists in adding a domain that rotates at the same speed as the propeller but in the opposite direction, thus a second cylinder was selected as this rotational domain. The simulation results remain the same. The real advantage of this method is that it reduces the computation time.

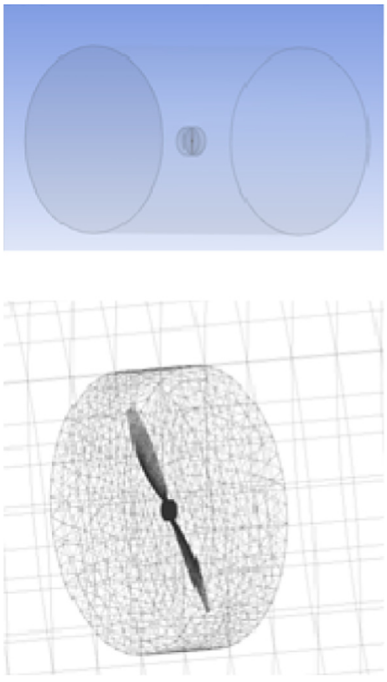

Fig. 12 Flow domain and mesh grid of the propeller for the CFD analysis.

A structured grid with a fine sizing relevance centre was used to mesh the propeller, and the flow domain. The CFD simulation was then performed to simulate the flow past the propeller under specific flight conditions. The flow dynamics was modelled with the same Eqs. (14)–(16) as the flow for the UAS aerodynamic sub-model.

In the second step, the Shear Stress Transport (SST) k-ω model was used to estimate the flow around the propeller. This model has been validated, and gave good results for turbomachinery blades, wind turbines and strong adverse pressure gradients in the boundary layer due to its rotation.[40] Thus, the SST k-ω could be very accurate for propeller analysis, and its equations were solved using ANSYS Fluent solver.

3.2. 2-stroke engine model

A two stroke engine is an internal combustion engine that produced torque or power from using a thermodynamic procedure. It is mainly composed by an inhaust system which is a carburettor, an exhaust system and a combustion chamber. The thermodynamic procedure that lead to the creation of torque append in the combustion chamber (Fig. 13).

In order to evaluate the performance of the two-stroke engine, the work produced has been separated into "ideal work" and "friction work".

The ideal work produced per cycle was carried out on the piston by the force F created from the gas pressure p[43]:

$$\text{Ideal work per cyle} = \int F\mathrm{d}x = \int pA\mathrm{d}x \int p\mathrm{d}V \tag{32}$$

where x is the distance covered by the piston and A is the piston area.

The ideal work of a two-stroke engine can be estimated from the Pressure-Volume diagram shown in Fig. 14 as the enclosed area of the diagram corresponding to the ideal Otto cycle.[45]

The Otto cycle, shown in Fig. 14, starts with the "intake phase" (1). The air flow passes through the carburettor where is mixed with fuel. The mix then enters into the combustion chamber to start the Otto cycle.

The pressure output of the carburettor which corresponds at the pressure at the intake phase is smaller than the atmospheric pressure depending on the admission valve opening controlled by the throttle. This pressure was estimated using:

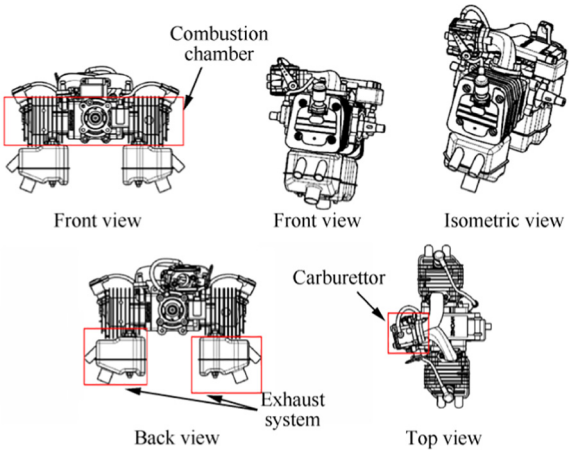

Fig. 13 2-stroke engine description.

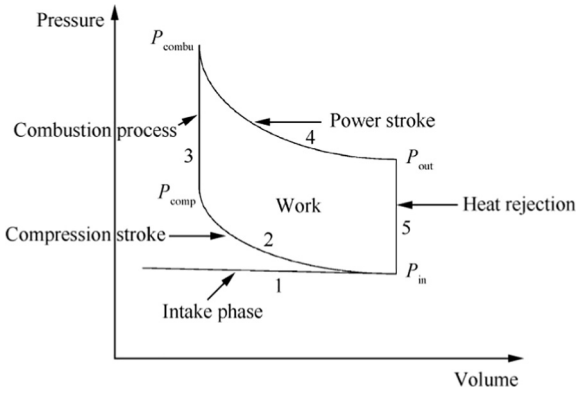

Fig. 14 Pressure-Volume diagram for the ideal Otto cycle.

$$P_{in} = [(P_{max} - P_{in})\text{Throt} + P_{min}]\frac{P_0}{P_{SL}} \tag{33}$$

where P_{in} is the pressure at the intake phase, P_0 is the atmospheric pressure, Throt is the throttle position from 0 to 1, P_{SL} is the pressure at sea level, P_{max} and P_{min} are the maximum and the minimum pressure delivered by the carburettor that correspond to the pressure for full open throttle and closed throttle. P_{max} is equal to the pressure at the sea level and, P_{min} is obtained with:

$$P_{min} = \frac{d_{venturi}}{d_{throttle\_bore}} P_{max} \tag{34}$$

where $d_{venturi}$ represents the diameter of the carburettor's Venturi, and $d_{throttle\_bore}$ is the diameter of the carburettor's throttle bore.

The mass rate of air mixture which enters in the combustion chamber is determined from:

$$\dot{m}_{air} = \rho A_s a = \rho A_s \left[\frac{2}{\gamma - 1}\left(\left(\frac{P_{in}}{P_0}\right)^{\frac{1}{\gamma}} - 1\right)\right] \tag{35}$$

where A_s is the swept volume of the cylinder of the engine, a is the velocity of the air particle, γ is the specific heat ratio.

The second phase of the cycle is the "compression stroke" (2). The piston moves from the down position to the top position. This motion leads to the augmentation of the pressure and the reduction of the volume occupied by the air-fuel mixture. The ratio of the volume at the beginning of compression to the volume at the end of compression is called the compression ratio. It is related to the pressure and the temperature according to:

$$P_{comp}/P_{in} = r_c^{\gamma} \tag{36}$$

$$T_{comp}/T_{in} = r_c^{\gamma - 1} \tag{37}$$

where r_c is the compression ratio, P_{comp} is the compression stroke pressure, T_{comp} is the compression stroke temperature.

The compression stroke is followed by a constant-volume heat input process called the "combustion stroke" (3). During this combustion phase, a large amount of energy is added to the cylinder. This energy increases the temperature of the air to very high values. This increase in temperature during a closed constant-volume process also results in a large increase in pressure[31] as seen also in:

$$T_{combu} = T_{comp} + \lambda Q / c_v \tag{38}$$

$$P_{combu} = P_{comp}(T_{combu}/T_{comp}) \tag{39}$$

where T_{combu} is the combustion temperature, P_{combu} is the combustion pressure, Q is the fuel heating value, c_v is the specific heat at constant volume, and λ is the air-fuel equivalence ratio, which is between 0.85 and 0.901 for the "octane". For the UAS' engine, the value of 0.85 was chosen.

The fuel flow per cycle and the fuel per time unit are thus estimated from:

$$\dot{m}_{fuelpercycle} = \dot{m}_{air}(\lambda / AFR_{stoich}) \tag{40}$$

$$\dot{m}_{fuel} = \dot{m}_{fuelpercylce}\omega_r \frac{1}{2\pi} N \tag{41}$$

where $\dot{m}_{fuelpercycle}$ is the fuel flow per cycle, $\dot{m}_{fuel}$ is the fuel flow per time unit, ω_r is the rotational speed of the engine, N is the number of cylinders of the engine, $\dot{m}_{air}$ is the mass rate of air, and AFR_{stoich} is the stoichiometric air fuel ratio, which is 15.05 for the octane.

The last phases of the Otto cycle are the "power stroke" (4) and the "heat rejection" (5). During the power stroke, the piston moves from the top position to the down position. The expansion ratio is the reciprocal of the compression ratio, and the same type of relationship can be used as the ones used during the compression stroke:

$$P_{out}/P_{combu} = r_c^{-\gamma} \tag{42}$$

$$T_{out}/T_{combu} = r_c^{1-\gamma} \tag{43}$$

At the "heat rejection" phase, the exhaust valve is opened and the residual passes through the exhaust system. The pressure is adjusted back to the intake pressure while the volume remains constant.

During the Otto cycle, the work is produced in the compression stroke and in the power stroke by the displacement of the piston. The work produced in a cycle is the difference between the work produced in the compression stroke and the work produced in the power stroke. The ideal work per cycle can thus be calculated using the difference of temperature between those phases:

$$W_i = c_v\left[(T_{combu} - T_{comp}) - (T_{in} - T_{out})\right] \tag{44}$$

where W_i is the ideal work produced.

The ideal power and the ideal torque produced by the engine are then estimated:

$$P_i = W_i \text{cps} \tag{45}$$

$$Q_i = P_i/\omega_r \tag{46}$$

where P_i is the ideal power produced by the engine, Q_i is the ideal torque produced by the engine, cps is the number of cycle per second.

The friction torque (and not the friction work) is calculated to obtain the torque produced by the engine. The friction torque is obtained by minimizing the error between the constructor data torque and the ideal torque as explained next. The proposed friction torque model is given in:

$$Q_f = k_1 + k_2\omega_r + k_3\omega_r^2 \tag{47}$$

where k_1, k_2, and k_3 are constants. The procedure to estimate these constants are divided into two steps. In the first step, a preliminary guess of these constant is obtained using the Least Square (LS) method. The results obtained are then used as initial conditions for the optimisation algorithm in the second step. This optimisation was used to find the constants k_1, k_2, k_3 for which the error between the constructor data and the ideal torque was minimized. The Nelder-Mead algorithm was used for this purpose.

Fig. 15 shows the overall engine model proposed for the UAS propulsion system. The model estimates the torque, the power and the fuel flow using as input the atmospheric pressure and temperature P_0 and T_{in}, the throttle position T_{hr}, the air density ρ, and the rotational speed of the crankshaft RPM.

The results obtained for each engine of the UAS-S4 and UAS-S45 were compared to the constructor data, and are presented in Section 6.

4. Actuator sub-model

The actuator system of the UAS-S4 and of the UAS-S45 is an HS7954SH servomotor is a controlled DC motor. Fig. 16 shows a schematic diagram of a DC motor.

The servomotor is controlled via the armature voltage e_a. The differential equation for the armature circuit is:

$$L_a\frac{di_a}{dt} + R_a i_a + e_b = e_a \tag{48}$$

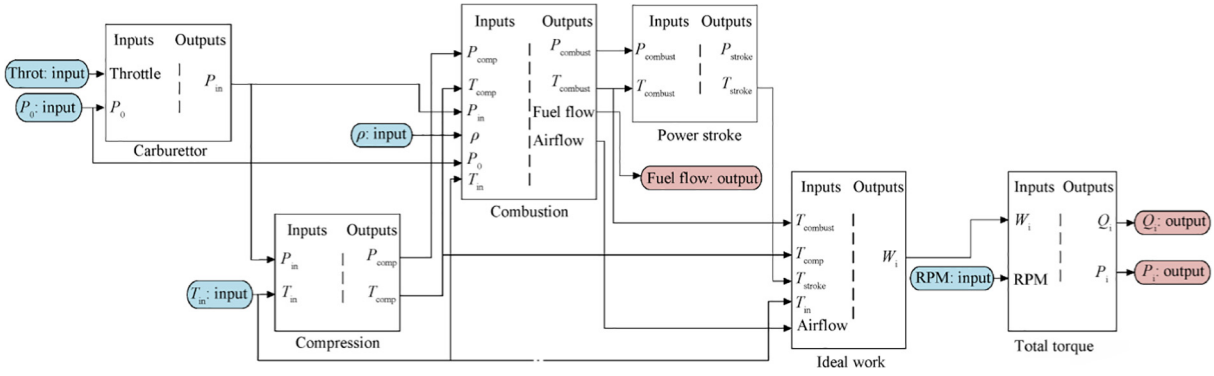

Fig. 15 Engine model proposed for the propulsion system of each UAS.

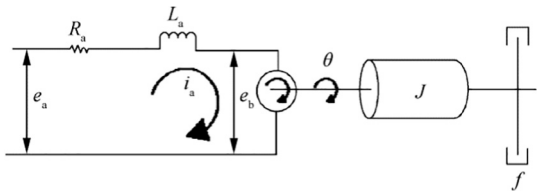

Fig. 16 Schematic diagram of a DC motor.

where the armature current intensity is given by i_a, L_a is the armature inductance, R_a is the armature resistance, and e_b is the back electromagnetic force which is proportional to the angular velocity $d\theta/dt$:

$$e_b = K_b \frac{d\theta}{dt} \tag{49}$$

where K_b is the DC motor's back electromagnetic force constant and θ is the angular displacement of the motor shaft.

The armature current delivers the torque, Q, relates to the inertia and the friction by a second order differential equation as shown in:

$$J\frac{d^2\theta}{dt^2} + f\frac{d\theta}{dt} = Q \tag{50}$$

where J is the inertia of the motor and f is the friction of the motor. The torque Q produced by the servomotor is directly proportional to the armature current intensity i_a:

$$Q = K_a i_a \tag{51}$$

where K_a is the motor's torque constant.

Applying the Laplace transform on Eqs. (48)–(51) leads to:

$$(L_a s + R_a) I_a(s) + E_b(s) = E_a(s) \tag{52}$$

$$\left(Js^2 + fs\right)\theta(s) = Q(s) \tag{53}$$

$$Q(s) = K_a I_a(s) \tag{54}$$

$$E_b(s) = K_b s\theta(s) \tag{55}$$

which can then be used to obtain the block diagram presented in Fig. 17.

A perturbation is added to the DC motor model which is the "hinge moment". The hinge moment is a resistive moment that the motor must overcome to move the control surface. It can be expressed using:

$$M_h = C_h \frac{1}{2}\rho V^2 S_e c_e \tag{56}$$

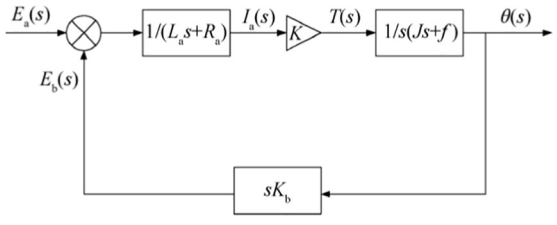

Fig. 17 Block diagram of DC motor system for each actuator.

where S_e is the area of the control surface, c_e is the chord of the control surface measured from the trailing edge of the flap and C_h is the hinge moment coefficient. The hinge moment coefficient is expressed by:

$$C_h = C_{h\alpha}\alpha + C_{h\delta}\delta \tag{57}$$

where $C_{h\alpha}$ is the hinge moment derivative due to the angle of attack, $C_{h\delta}$ is the hinge moment derivative due to the control surface deflection, δ is the control surface deflection and α is the angle of attack.

For the case of the elevator, the angle of attack is expressed by:

$$\alpha_t = \alpha_w - i_w - \varepsilon + i_t \tag{58}$$

where α_t is the angle of attack of the horizontal tail, α_w is the angle of attack of the wing, i_w is the incidence angle of the wing, i_t is the incidence angle of the horizontal tail, ε is the downwash angle.

All of the useful parameters such as the armature resistance, R_a, the armature inductance, L_a, the inertia, J, and the friction, f, of the motor, in the DC motor block diagram (Fig. 16) can be found in manufacturers' datasheets. To obtain a servomotor model, a PID controller was added to the DC motor model (Fig. 17). The PID controller was tuned such that the resultant servomotor model has the same operation speed as the one in the manufacturer's documentation in absence of perturbation. Therefore, for the PID tuning, the hinge moment M_h (normally considered as perturbation) was assumed to be zero.

In addition, the inductance armature L_a, is very small and can be neglected. The servomotor is also assumed to have no electromagnetic losses, thus the torque constant K_a is equal to back electromagnetic force constant K_b:

$$K_a = K_b = K \tag{59}$$

The system of Eqs. (52)–(55) can be reduced to the opened loop transfer function:

$$\frac{\Theta(s)}{E_a(s)} = \frac{K}{s(R_a J)s + R_a f + K^2} = \frac{G}{s(T_s s + 1)} \tag{60}$$

where

$$G = \frac{K}{R_a f + K^2} = \text{motor gain constant} \tag{61}$$

$$T_s = \frac{R_a J}{R_a f + K^2} = \text{motor time constant} \tag{62}$$

The closed loop transfer function of the DC motor is obtained from Eq. (63) and is expressed by:

$$F(s) = \frac{\omega_a^2}{s^2 + 2\xi\omega_a s + \omega_a^2} \tag{63}$$

where $\omega_a = \sqrt{\frac{kG}{T_s}}$ is the natural frequency of the system, and $\xi = \frac{1}{2T_s\omega_a}$ is the damping ratio of the system, k is the maximum voltage of the servomotor. It is added to convert the desired angle into a voltage.

The resulting servomotor block diagram is shown in Fig. 18 and he tuning of the PID controller was performed using MATALB/Simulink toolbox.

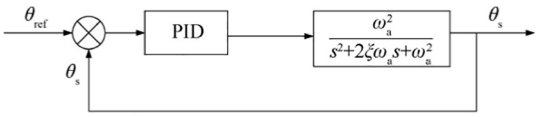

Fig. 18 Block diagram of the servomotor system for each actuator.

5. Structural analysis

The structural analysis includes the estimation of the mass, the center of gravity, and the inertia of each UAS. Numerical and experimental analyses to calculate the mass and the center of gravity of the UAS-S4 were performed recently at our laboratory LARCASE, ETS and are explained in.[44–46] The experimental tests were used to validate the numerical code and analysis. The numerical code, following its experimental validation on the UAS-S4, was further applied on the UAS-S45.

The UAS-S45 structure was divided into six components: the wings, the fuselage, the power plants, the vertical tail, the horizontal tail and the landing gear. Each component was replaced by basic shapes such as triangles, rectangles and trapezoids to facilitate the calculation of its center of gravity and mass,[47] see Fig. 19.

Using the classification of the UAS-S45, the equations provided by Raymer[22] were applied on each of its components to estimate its weight.

The estimation of the wing mass is shown as an example. The UAS-S45 has a straight-tapered wing which can be approximated by a trapezoid on the top view, and a diamond-shaped on the side view (Fig. 20).

The Raymer equation for the estimation of the wing mass W_w is given by:

$$W_w = 0.036 S_w^{0.758} \left(\frac{AR}{\cos^2(\Lambda_{c/4})}\right)^{0.6} q^{0.006} \lambda^{0.04} \cdot \left(\frac{100 t/c}{\cos(\Lambda_{c/4})}\right)^{-0.3} (n_z W_o)^{0.49} \tag{64}$$

where AR is the aspect ratio of the wing, $\Lambda_{c/4}$ is the wing sweep at 25% of the mean geometric chord, q is the dynamic pressure at cruise, t/c is the wing thickness to chord ratio, λ is the wing taper ratio, n_z is the ultimate load factor, which is 5 for a general class aviation airplane or default aircraft, and W_o is the designed gross weight.

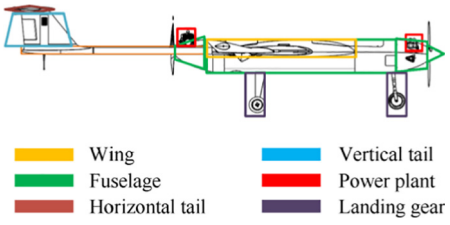

Fig. 19 UAS-S45 decomposition using basic shapes.

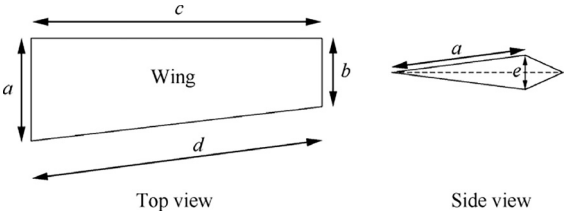

Fig. 20 Top view and side view of the UAS-S45 wing using basic shapes.

The parameters such as AR, $\Lambda_{c/4}$, λ, and t/c are given by:

$$\lambda = \frac{a}{b} \tag{65}$$

$$\Lambda_{c/4} = \tan^{-1}\left(\frac{0.75(a-b)}{c}\right) \tag{66}$$

$$\frac{t}{c} = \frac{e}{a} \tag{67}$$

$$AR = 4\frac{c^2}{S_w} \tag{68}$$

The center of gravity location of each component was estimated using Mechanical Engineering calculations applied to the basic shapes. The center of gravity location of the whole UAS was then calculated using the weighted arithmetic mean of the center of gravity locations of each of its components.

$$x_{cg} = \frac{\sum x_{cgi} m_i}{\sum m_i} \tag{69}$$

$$y_{cg} = \frac{\sum y_{cgi} m_i}{\sum m_i} \tag{70}$$

$$z_{cg} = \frac{\sum z_{cgi} m_i}{\sum m_i} \tag{71}$$

where x_{cgi}, y_{cgi} and z_{cgi} are the center of gravity locations of each component of the UAS, and m_i is the mass of each component.

To obtain the inertia of the UAS-S4, Tondji and Botez[46] developed a methodology based on the DATCOM code. The methodology consists of dividing the aircraft into five major components: wings, fuselage, horizontal stabilizer, vertical stabilizer and power plant. The inertia of each component was calculated about its center of gravity. The total aircraft inertia about its main axis is given by equations:

$$I_x = \sum \left(m_i x_{cgi}^2 + I_{oxi}\right) \tag{72}$$

$$I_y = \sum \left(m_i y_{cgi}^2 + I_{oyi}\right) \tag{73}$$

$$I_z = \sum \left(m_i z_{cgi}^2 + I_{ozi}\right) \tag{74}$$

where I_{oxi}, I_{oyi} I_{ozi} are the inertia values of each component about their center of gravity, and I_x, I_y I_z are the inertia values about the main axis of the UAS. The inertia about the center of gravity of the UAS can then be obtained from the Huygens theorem.[46] The same method was applied to estimate the inertia of the UAS-S45.

6. Results and discussion

Relative error: The relative error between a reference value x_a and an approximated value x_b is calculated as relative error $= \left|\frac{x_b - x_a}{x_a}\right| \times 100\%$.

6.1. Aerodynamic sub-model

Fderivatives in-house code does not take into account the parallel vertical tails and the winglets that are components of our UAS (see Fig. 21). The parallel vertical tails of each UAS were then replaced in this code by a single vertical tail with a double reference area. It was thus possible to use the CFD analysis to estimate the contributions of the parallel vertical tails. For the UAS-S45, the winglets were not modelled, and their contributions to the whole UAS have been neglected for the validation.

The flight conditions were considered as function of the altitudes, Mach numbers and angles of attack. The range of these parameters values associated with each flight condition is presented in Table 4. The unknown aerodynamic coefficients (lift, drag and pitch) can be found by interpolation, for any flight condition based on this range of flight conditions parameter values.

Fig. 22 shows the comparison of the lift, drag and pitch moment coefficients estimated with Fderivatives, DATCOM and TORNADO for the UAS-S4. The range of the angle of attack was reduced to [−8°, 12°] because the CFD analysis with ANSYS Fluent predicted the beginning of the stall at 10° while Fderivatives and DATCOM codes estimated a linear lift coefficient variation with angle of attack until 17°. The three semi-empirical methodologies (Fderivatives, DATCOM and TORNADO) gave very close results for C_L and C_m. In the same way as with the UAS-S45, the highest difference

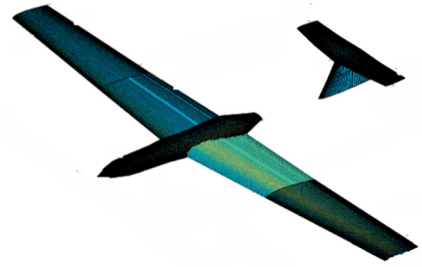

(a) UAS-S4

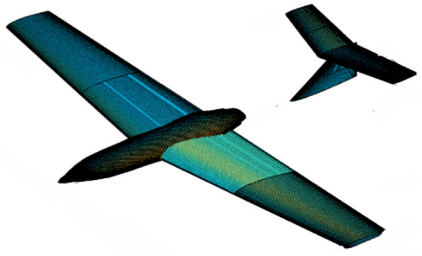

(b) UAS-S45

Fig. 21 Model of the UAS-S4 and the UAS-S45 performed with Fderivatives code.

Table 4 Flight conditions for the aerodynamic coefficients determination.

Altitude (ft)	*Ma*	Angle of attack (°)
0–20000	0.1–0.2	−17–17

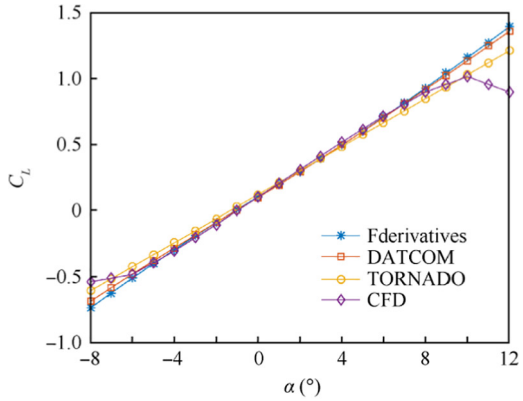

(a) Lift coefficient

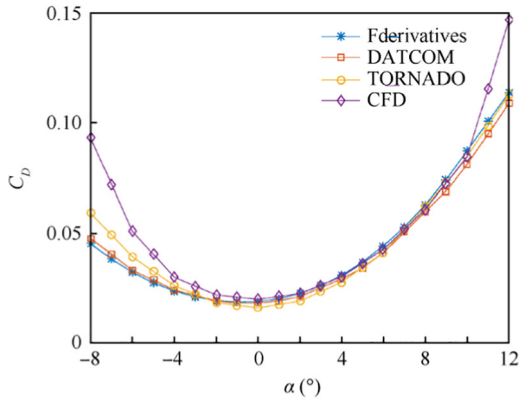

(b) Drag coefficient

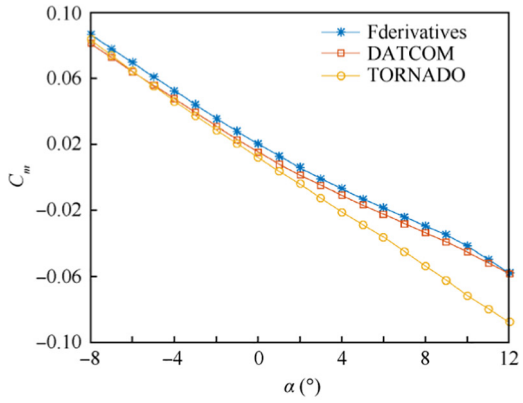

(c) Pitch moment coefficient

Fig. 22 Lift, drag and pitch moment coefficient variation with the angle of attack for the UAS-S4 at altitude = 10000 ft and Mach number = 0.14.

can be observed in the estimation of the pitching moment coefficient at high positive angles of attack with TORNADO code.

A comparison of the lift, drag and pitch moment coefficients estimated with Fderivatives, DATCOM and TORNADO codes for the UAS-S45 is shown in Fig. 23. The estimation was performed for an altitude of 10000 ft. and a Mach number of 0.14. It can be seen that there is reasonable agreement between the three methodologies results on the lift and drag coefficients. The difference in results is associated with the estimation of the drag coefficient with TORNADO. This difference is probably due to no evaluation method for

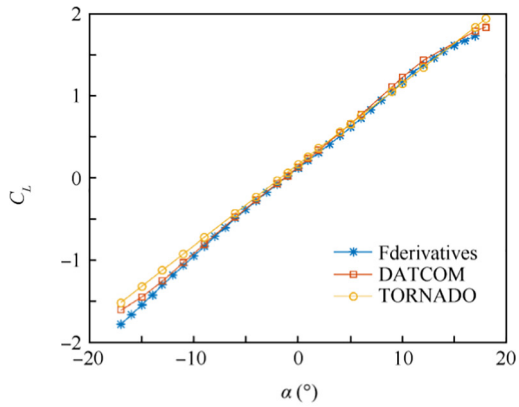

(a) Lift coefficient

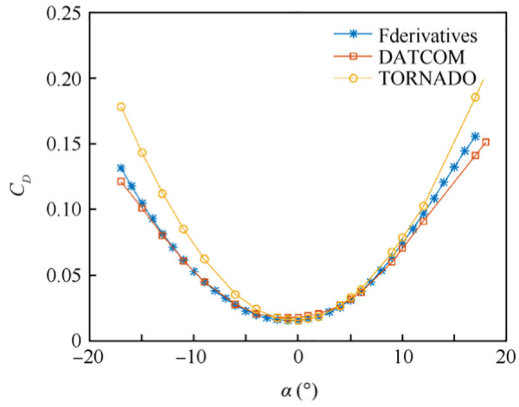

(b) Drag coefficient

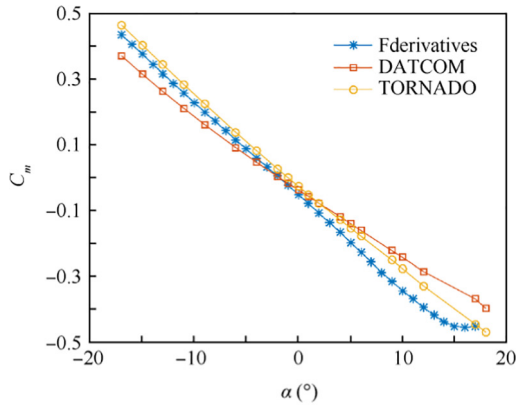

(c) Pitch moment coefficient

Fig. 23 Lift, drag and pitch moment coefficient variation with the angle of attack for the UAS-S45 at altitude = 10,000 ft and Mach number = 0.14.

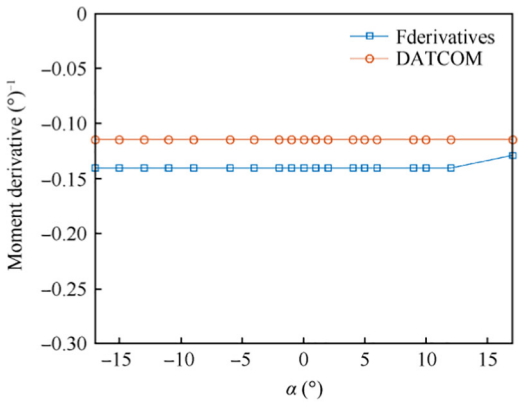

(a) Moment derivative

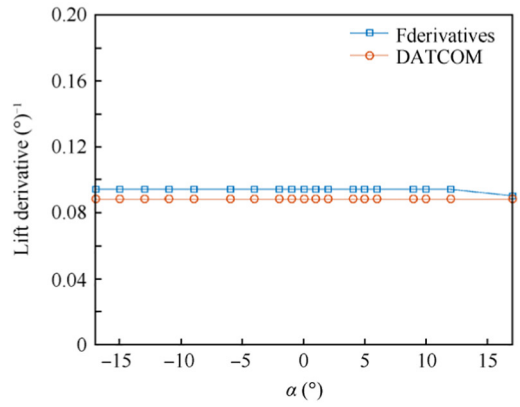

(b) Lift derivative

Fig. 24 Lift and moment derivative with respect to pitch rate variation with the angle of attack for the UAS-S45 at altitude = 15,000 ft, Mach number = 0.18.

the contribution of the fuselage. Because of the lack of a method to evaluate the contribution of the fuselage in TORNADO, the calculation of the longitudinal and lateral stability derivatives was validated using only DATCOM and Fderivatives codes.

Fig. 24 displays the longitudinal lift and moment derivatives with respect to pitch rate with angle of attack, for the UAS-45 (Mach number of 0.18, altitude of 15000 ft). Both Fderivatives and DATCOM codes estimated constant lift and moment derivatives with respect to pitch rate. There is a rather good agreement between DATCOM and Fderivatives on the lift derivative with respect to pitch rate, with a difference of 6.36% equivalent to a relative error, but the difference is higher for the moment derivative with respect to pitch rate (Fig. 24).

Figs. 25–27 show a comparison of lateral derivatives variations with angle of attack calculated with Fderivatives and DATCOM codes. These estimations were performed for an altitude of 10000 ft. and a Mach number of 0.18. Fderivatives code results clearly show a good agreement with the DATCOM results especially for angles of attack between −10° and 12°. The results remain the same for the other flight conditions.

6.2. Propulsion sub-model

The UAS-S4 and the UAS-S45 use the same 18 inch MEJZLIK propeller. The Blade Element Theory (BET) was applied to the 18 inch propeller of each UAS for different values of speeds and attitudes. Fig. 28 shows the variation of the thrust obtained as a function of the speed and the altitude. As seen on Fig. 28, as both the altitude and the speed increase, the generated thrust decreases. The maximum thrust, also known as the static thrust, is obtained at the ground (altitude = 0 ft), thus at zero speed.

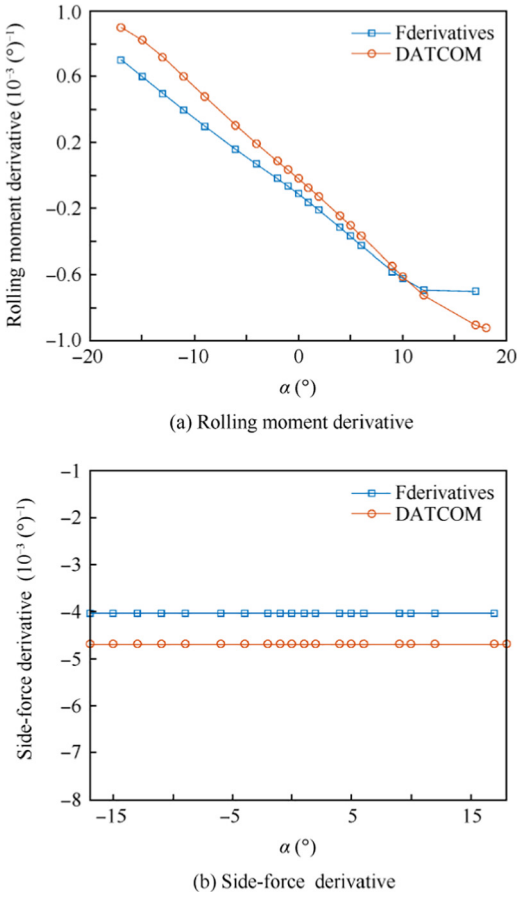

Fig. 25 Side-force and rolling moment derivative coefficients with respect to sideslip angle, β, as function of angle of attack at altitude = 15,000 ft, Mach number = 0.18.

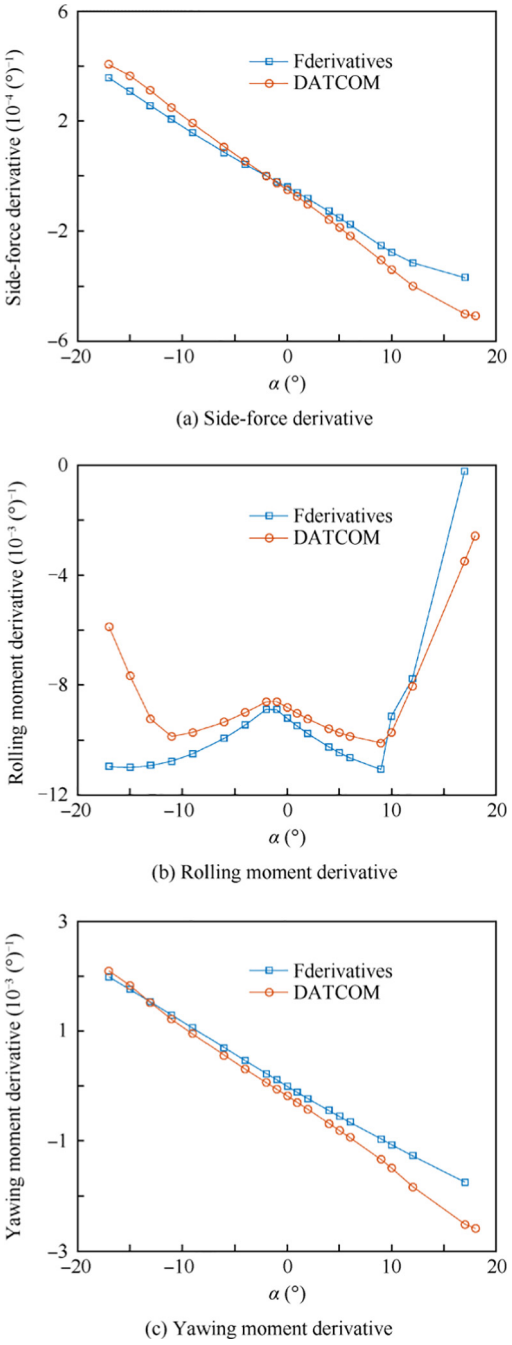

Fig. 26 Side-force, rolling and yawing moment derivatives with respect to the roll rate as function of the angle of attack at altitude = 15,000 ft, Mach number = 0.18.

Fig. 29 presents the thrust coefficient C_T and the propeller efficiency η variations with the advance ratio obtained with the BET, and with the CFD analysis using ANSYS Fluent. The results are obtained as function of the Advance Ratio, which is an adimensional parameter, defined as the ratio of the free-stream fluid to the propeller tip speed and were evaluated at an altitude of 10000 ft as in Eq. (31). Fig. 29 shows that there is a reasonable agreement between these results obtained with two methodologies. The maximum relative error for the thrust coefficient is 5.6%, while for the propeller efficiency is 10.28%.

In the case of the 2-stroke engine, the torque produced by the proposed engine model (Fig. 15) was compared to the torque provided by the manufacturer's documentation. Each UAS has two engines: the ZENOAH G800BPU at its front and the ZENOAH G620BPU at its rear. Fig. 30 shows the comparison of the real values of the torque with their estimations for each engine given in Section 3.

Fig. 30 demonstrates the close agreement between the estimated torque and its real value for each engine, with a mean relative error of 1.56% for the ZENOAH G800BPU, and 0.83% for the Zenoah G620BPU.

6.3. Actuator sub-model

As specified in Section 4, the actuator sub-model, which is a servomotor, was estimated using controlled DC motor. The transfer function from Eq. (63) was used with $\omega_a = 1.1636$ rad/s and $\xi = 0.0163$ defining the system natural frequency and the damping ratio, respectively. The PID controller was tuned to obtain a desired operating speed when the hinge moment was zero. The servomotor HS7954SH has an operating speed of 0.1 s/60°, as specified in the datasheet. To meet this specification, the tuning of the PID controller was performed using MATALB/Simulink toolbox.

Fig. 31 shows the tuning of the PID controller, the operating time of servomotor, which is the servomotor to reach its final position, is similar to the settling time. For this purpose

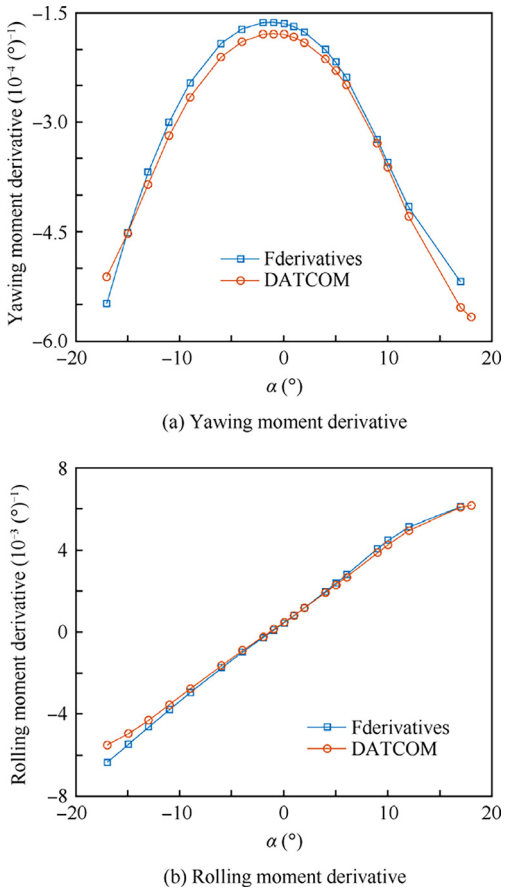

(a) Yawing moment derivative

(b) Rolling moment derivative

Fig. 27 Rolling and yawing moment derivatives with respect to the yaw rate as function of the angle of attack at altitude = 15000 ft, Mach number = 0.18.

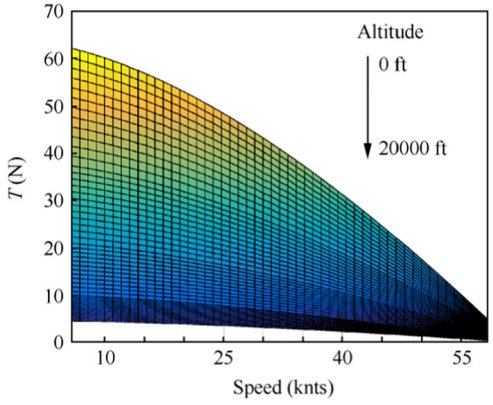

Fig. 28 Thrust variation with speed and altitude.

the PID controller was tuned to obtain a settling time of 0.1 s. The estimated controller parameters were $P = 19.54$, $I = 241.81$, $D = 0.37$. A step response procedure was performed to validate the actuator sub-model. The settling speed of the servomotor was compared to the manufacturer's operation speed 0.1 s/60°.

Fig. 32 shows the excellent results obtained for the step response of 60°. Therefore, the response time obtained was

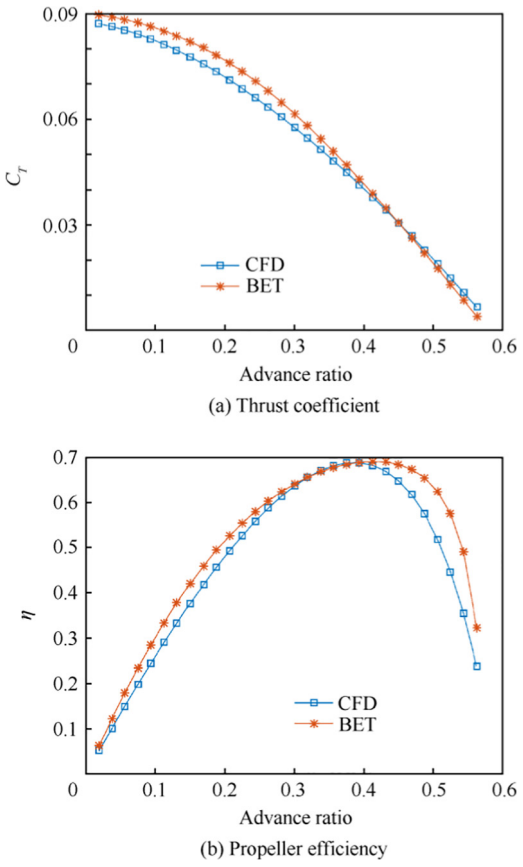

(a) Thrust coefficient

(b) Propeller efficiency

Fig. 29 Thrust coefficient and propeller efficiency variation with the advance ratio for the altitude of 10,000 ft.

similar to the operating speed specified by the manufacturer s seen on Fig. 32.

6.4. Structural analysis

Tondji and Botez[47] performed a structural analysis of the Unmanned Aerial System UAS-S4. They estimated numerically the mass, position of the center of gravity and the moment of inertia numerically from the Raymer and DATCOM methods and further validated the results using and experimental pendulum method. The Raymer and DATCOM methods were applied to the UAS-S4 which was initially divided into components as fuselage, wing, and tail. Each component was approximated to basic shapes (triangle, square, circle etc.). The mass of each component as well as the mass of the entire UAS-S4 was then calculated by applying equations from the Raymer methods. The center of gravity results from the mass estimation using Eqs. (69)–(71). The moment of inertia of each component was calculated using DATCOM equations and then the overall UAS-S4 was computed from the Huygens theorem.[47] The mass of the UAS-S4 was validated experimental using results of an accurate scale. The center of gravity and the moment of inertia were validated using results from a pendulum method. For this purpose, the UAS-S4 was installed on a pendulum and the rotational angle and speed were measured. The data measured led to the development of a nonlinear dynamic model for the rotational motion of the pendulum. The center of gravity and the moment of inertia

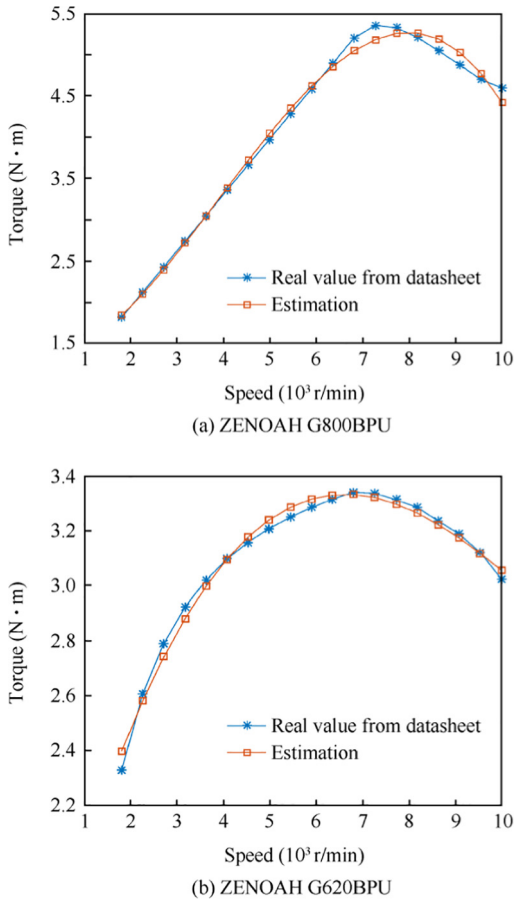

Fig. 30 Torque variation with the speed for the ZENOAH G800BPU and ZENOAH G620BPU.

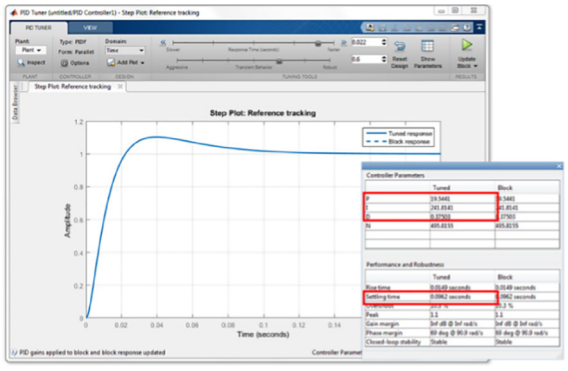

Fig. 31 PID controller tuning using MATLAB/Simulink toolbox.

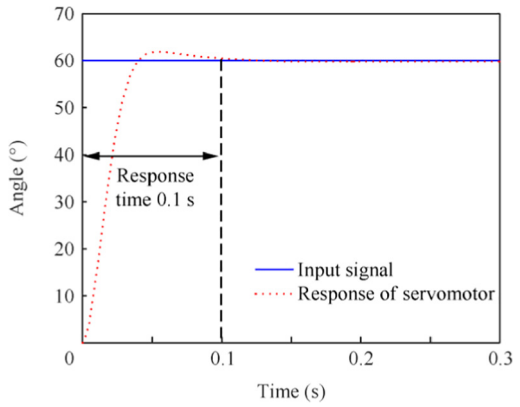

Fig. 32 Step response of the servomotor model for a signal of 60°.

were thus extracted from this model. The comparison between numerical and experimental data showed relative errors of 5.5%, 1.14% and 1.184% respectively for the x, y and z positions on the center of gravity. The moment of inertia from the DATCOM method was also compared to those obtained using the pendulum method. The relative errors were 15.69%, 1.84% and 2.05% for the inertia about the x axis, y axis and z axis.

The results obtained for the mass, the center of gravity and the inertia analyses are presented in Table 5. The unloaded mass of the UAS-S45 is 121.25 lb and its maximum mass is 153 lb. Thus, it allows 31.75 lb for the fuel, and for the extra load, such as a camera. To obtain the results presented in Table 4, the center of gravity and the inertia analyses were evaluated for a range of mass between than the UAS-S45 maximum mass (167.79 lb) and its unloaded mass (117.79 lb) by changing adequately the fuel and the extra load masses. These considerations were made to avoid extrapolation when calculating values of center of gravity and inertia for a UAS-S45 mass near to the mass extremities such as the maximum mass or to the unloaded mass.

By knowing the fuel flow of each UAS, any position of the center of gravity and inertia can be interpolated from Table 5. To validate the results obtained, the unloaded mass of the UAS-S45 and its corresponding position of the center of gravity for the unloaded mass were estimated. The unloaded mass of the UAS-S45 was calculated by applying the Raymer's equations as specified in Section 5 in the absence of fuel and extra load. The corresponding center of gravity was interpolated using Table 5. These values were compared with real center of gravity data of the UAS-S45, as shown in Table 6. The estimated results show a very close agreement with the real data with a relative error of 0.07% for the mass and 5.7% for the x-position of the center of gravity.

Table 5 Data obtained from the structural analysis for UAS-S45.

Mass (lb)	167.79	157.79	147.79	137.79	127.79	117.79
x_{cg} (in)	43.7676	44.0652	44.3796	44.7396	45.1536	45.6360
z_{cg} (in)	16.5360	16.6620	16.7952	16.9488	17.1240	17.3292
I_{xx} (10^4lb·in^2)	9.9266	9.9367	9.9278	9.9187	9.9087	9.874
I_{yy} (10^4lb·in^2)	6.7060	6.7797	6.6898	6.5933	6.4885	6.1904
I_{zz} (10^5lb·in^2)	1.6695	1.675	1.6663	1.6570	1.647	1.6201

Note: 1 lb = 0.45359 kg; 1 in = 25.4 mm.

Table 6 Comparison of mass and position of center of gravity estimated with the real values.

Parameter	Unloaded mass (lb)	x_{cg} (in)	z_{cg} (in)
Estimation	121.34	45.63	4.24
Real value from datasheet	121.25	48.43	4.15
Error (%)	0.07	5.7	2.1

7. Conclusions

A modelling procedure for the UAS-S4 and the UAS-45 was presented in this paper. The overall model of each UAS was divided into four sub-models, and the estimation methods of each sub-model were detailed. The aerodynamic sub-model was obtained from geometrical data using the in-house code Fderivatives, the DATCOM procedure, TORNADO and a CFD analysis on ANSYS-Fluent. The propulsion sub-model was estimated by coupling a two-stroke engine model based on the ideal Otto cycle with a blade element theory analysis on the propeller. The mass, the inertia and the position of the center of gravity were determined from the Raymer and the DATCOM methodologies. The actuator system was estimated from a DC servomotor model controlled with a PID controller.

A validation was performed for each sub-model. The aerodynamic sub-model obtained using Fderivatives was compared with CFD-Fluent analysis, a Vortex Lattice Method (VLM) and the DATCOM procedure. The propeller sub-model estimate using the Blade Element Theory (BET) was compared with CFD-Fluent analysis. The engine sub-model, the actuator sub-model, the mass and the center of gravity was compared with experimental data. The results show good agreement for each sub-model with respect to its experimental sub-model. The complete UAS-S4 and UAS-S45 simulation models were assembled on Matlab/Simulink, and thus can be useful for efficient flight dynamics and control laws modelling and simulation technologies. The intent is to design a level D (highest level of flight dynamics) simulator for these UAS-S4 and US-S45 that will be validated with experimental flight test data.

Acknowledgements

Special thanks are dues to the Natural Sciences and Engineering Research Council of Canada (NSERC) for the Canada Research Chair Tier 1 in Aircraft Modelling and Simulation Technologies funding. We would also like to thank Mrs. Odette Lacasse and Mr. Oscar Carranza for their support at the ETS, as well as to Hydra Technologies' team members Mr. Carlos Ruiz, Mr. Eduardo Yakin and Mr. Alvaro Gutierrez Prado in Mexico.

References

1. Liu Z, He Y, Yang L, Han J. Control techniques of tilt rotor unmanned aerial vehicle systems: A review. *Chinese Journal of Aeronautics* 2017;**30**(1):135–48.
2. Kamal AM, Bayoumy AM, Elshabka AM. Modeling and flight simulation of unmanned aerial vehicle enhanced with fine tuning. *Aerospace Science and Technology* 2016;**51**:106–17.
3. Jodeh NM, Blue P, Waldron A. Development of small unmanned aerial vehicle research platform: Modeling and simulating with flight test validation. *AIAA modeling and simulation technologies conference and exhibit*. Reston: AIAA; 2006.
4. Al-Radaideh A, Al-Jarrah MA, Jhemi A, Dhaouadi R. ARF60 AUS-UAV modeling, mystem identification, guidance and control: Validation through hardware in the loop simulation. *6th international symposium on mechatronics and its applications*. 2009. p. 1–11.
5. Selig MS. Real-time flight simulation of highly maneuverable unmanned aerial vehicles. *Journal of Aircraft* 2014;**51**(6):1705–25.
6. Selig MS. Aerodynamic design software for horizontal axis wind turbines [dissertation]. Urbana: Aerospace Engineering University of Illinois; 2012.
7. Elharouny AS, Youssef AM, Zakaria MY, Abdel-Hameed MM. Procedures for mathematical modeling for small unmanned aerial vehicles. *Proceedings of the 15th AMME conference*; 2012. p. 1.
8. Drela M. XFOIL: An analysis and design system for low Reynolds number airfoils. *Low Reynolds number aerodynamics*. Berlin, Heidelberg: Springer; 1989. p. 1–12.
9. Raymer DP. A computer-aided aircraft configuration development system. *17th aerospace sciences meeting*. Reston: AIAA; 1979.
10. Roskam J. *Airplane flight dynamics and automatic flight controls*. DARcorporation; 1998.
11. Roskam J. *Airplane design: Preliminary sizing of airplanes*. DARcorporation; 1985.
12. Roskam J. *Airplane design VII: Determination of stability, control and performance characteristics: FAR and Military Requirements*. DARcorporation; 1985.
13. Raymer DP, McCrea MM. Design of jet STOVL aircraft using RDS-professional. 2010. p. 8.
14. Williams JE, Vukelich SR. The USAF stability and control digital datcom. Volume i. users manual. *USAF stability & control digital datcom*. 1979.
15. Rocca GL, Van Tooren MJL. Knowledge-based engineering approach to support aircraft multidisciplinary design and optimization. *Journal of Aircraft* 2009;**46**(6):1875–85.
16. Morris A. MOB A European distributed multi-disciplinary design and optimisation project. *9th AIAA/ISSMO symposium on multidisciplinary analysis and optimization*. Reston: AIAA; 2002.
17. Cerulli C, Schut EJ, Berends JPTJ, Van Tooren MJL. Tail optimization and redesign in a multi agent task environment (TAILORMATE). *47th AIAA/ASME/ASCE/AHS/ASC structures, structural dynamics, and materials conference*. Reston: AIAA; 2006.
18. Schut J, Tooren MV. Design "feasilization" using knowledge-based engineering and optimization techniques. *Journal of Aircraft* 2007;**44**(6):1776–86.
19. Rizzi A. Modeling and simulating aircraft stability and control—The SimSAC project. *Progress in Aerospace Sciences* 2011;**47**(8):573–88.
20. Howe D. *Aircraft conceptual design synthesis*. London: Professional Engineering Publishing; 2000.
21. Torenbeek E. The wing structure and its weight. *Advanced aircraft design: conceptual design, analysis and optimization of subsonic civil airplanes*. Chichester: John Wiley & Sons, Ltd; 2013. p. 319–62.
22. Raymer DP. *Aircraft design: a conceptual approach*. Reston: AIAA; 1989.
23. Jodeh NM. Development of autonomous unmanned aerial vehicle platform: modeling, simulating, and flight testing [dissertation]. Ohio: Air Force Institute of Technology; 2006.
24. Sugar Gabor O. Validation of morphine wing methodologies on an unmanned aerial system and a wind tunnel technology demonstrator [dissertation]. Montréal: École de Technologie Supérieure; 2015.
25. Anton N, Botez RM, Popescu D. Stability derivatives for a delta-wing X-31 aircraft validated using wind tunnel test data. *Proceedings of the Institution of Mechanical Engineers, Part G: Journal of Aerospace Engineering* 2011;**225**(4):403–16.

26. Hua J, Zheng S, Zhong M, WANG GL, Eitelberg G, Hegen S, et al. Recent development of a CFD-wind tunnel correlation study based on CAE-AVM investigation. *Chinese Journal of Aeronautics* 2018;**31**(3):419–28.
27. Bertin JJ, Smith ML. *Aerodynamics for engineers*. New Jersey: Prentice-Hall; 1998.
28. Anton N, Botez RM, Popescu D. New methodologies for aircraft stability derivatives determination from its geometrical data. *AIAA atmospheric flight mechanics conference*. Reston: AIAA; 2009.
29. Anton N, Botez RM, Popescu D. New methodology and code for hawker 800XP aircraft stability derivatives calculation from geometrical data. *The Aeronautical Journal* 2010;**114**(1156): 367–76.
30. Popescu D. Nouvelle implementation de la procédure DATCOM pour le calcul des coefficients aerodynamiques et des derivees de stabilite dans le domaine subsonique de vol [dissertation]. Montréal: École de Technologie Supérieure; 2009.
31. Kinsey DW, Bowers DL. *A computerized procedure to obtain the coordinates and section characteristics of NACA designated airfoils*. Ohio: Air Force Flight Dynamics Lab Wright-Patterson; 1971.
32. Pankhurst RC. *A method for the rapid evaluation of Glauert's expressions for the angle of zero lift and the moment at zero lift*. London: H.M. Stationery Office; 1944.
33. Jacobs EN, Ward KE, Pinkerton RM. *The characteristics of 78 related airfoil sections from tests in the variable-density wind tunnel*. Washington, D.C.: NASA; 1933.
34. Phillips WF, Alley NR. Predicting maximum lift coefficient for twisted wings using lifting-line theory. *Journal of Aircraft* 2007;**44** (3):898–910.
35. Whitcomb RT. *A study of the zero-lift drag-rise characteristics of wing-body combinations near the speed of sound*. Washington, D.C.: NASA; 1952.
36. Kuitche M, Botez RM. Methodology of estimation of aerodynamic coefficients of the UAS-E4 ehécatl using datcom and VLM procedure. *AIAA modeling and simulation technologies conference*. Reston: AIAA; 2017.
37. Şugar Gabor O, Koreanschi A, Botez RM. A new non-linear vortex lattice method: applications to wing aerodynamic optimizations. *Chinese Journal of Aeronautics* 2016;**29**(5):1178–95.
38. Moran J. *An introduction to theoretical and computational aerodynamics*. New York: Courier Corporation; 1984.
39. Şugar Gabor O, Koreanschi A, Botez RM, Mahmoud M, Mebarki Y. Numerical simulation and wind tunnel tests investigation and validation of a morphing wing-tip demonstrator aerodynamic performance. *Aerospace Science and Technology* 2016;**53**:136–53.
40. Argyropoulos CD, Markatos NC. Recent advances on the numerical modelling of turbulent flows. *Applied Mathematical Modelling* 2015;**39**(2):693–732.
41. Menter FR. Two-equation eddy-viscosity turbulence models for engineering applications. *AIAA Journal* 1994;**32**(8):1598–605.
42. Gudmundsson S. *General aviation aircraft design: applied methods and procedures*. Boston: Butterworth-Heinemann; 2013.
43. Blair GP. *Design and simulation of two stroke engines*. Warrendale: SAE International; 1996.
44. Communier D, Salinas Flores M, Carranza Moyao O, Botez RM. Aero structural modeling of a wing using CATIA V5 and XFLR5 software and experimental validation using the Price- Païdoussis wing tunnel. *AIAA atmospheric flight mechanics conference*. Reston: AIAA; 2015.
45. Tondji Y, Botez RM. Semi-empirical estimation and experimental validation of the mass and the center of gravity location of the unmanned aerial system – UAS-S4 of hydra technologies. *2016 international conference on unmanned aircraft systems (ICUAS)*. 2016. p. 1319–26.
46. Tondji Y, Botez RM. Semi-empirical estimation and experimental method for determining inertial properties of the unmanned aerial system – UAS-S4 of hydra technologies. *The Aeronautical Journal* 2017;**121**(1245):1648–82.
47. Chahbani S. Estimation des masses, des centres de Gravité ainsi que des Moments d'Inertie de l'Avion Cessna Citation X [dissertation]. Montréal: École de technologie supérieure; 2015.